J. Fluid Mech. (1988), *vol.* 194, *pp.* 479–510
Printed in Great Britain

Oscillations of drops in zero gravity with weak viscous effects

By T. S. LUNDGREN† AND N. N. MANSOUR‡

†Department of Aerospace Engineering and Mechanics, University of Minnesota,
Minneapolis, MN 55455, USA

‡NASA Ames Research Center, Moffett Field, CA 94035, USA

(Received 21 August 1987 and in revised form 26 January 1988)

Nonlinear oscillations and other motions of large axially symmetric liquid drops in zero gravity are studied numerically by a boundary-integral method. The effect of small viscosity is included in the computations by retaining first-order viscous terms in the normal stress boundary condition. This is accomplished by making use of a partial solution of the boundary-layer equations which describe the weak vortical surface layer. Small viscosity is found to have a relatively large effect on resonant-mode coupling phenomena.

1. Introduction

Motivated by the importance of containerless processing technology in space (Carruthers & Testardi 1983), we present a numerical study of nonlinear oscillations and other motions of large unsupported liquid drops in zero gravity. When gravity is negligible the liquid will tend to form spherical drops to minimize the surface energy. These drops will vibrate under the influence of external forces and, in the absence of a surrounding fluid, the only source of damping is the weak viscous effects generated in a thin layer along the surface of the drop.

Lamb (1932, §275) presents Rayleigh's (1879) linearized solution for small 'vibrations of a globule'. The axially symmetric form of the solution is the superposition of modes of form

$$r = a + \epsilon_n P_n(\cos\Theta)\sin(\omega_n^0 t + \eta) \tag{1.1}$$

for the surface shape, and

$$\phi = -\frac{\omega_n^0 a}{n}\left(\frac{r}{a}\right)^n \epsilon_n P_n(\cos\Theta)\cos(\omega_n^0 t + \eta) \tag{1.2}$$

for the velocity potential inside the drop, and the frequencies ω_n^0 are given by

$$(\omega_n^0)^2 = \frac{n(n-1)(n+2)T}{\rho a^3}. \tag{1.3}$$

T is the surface tension, a is the unperturbed radius of the drop, and $P_n(\cos\Theta)$ is the Legendre polynomial of order n with Θ the polar angle.

Analysis of slightly nonlinear drop oscillations has been carried out by Tsamopoulos & Brown (1983) who showed, among other things, that the nonlinearity is 'soft'. The frequencies of the first four modes were shown to decrease with increasing amplitude. This has been verified quantitatively for the second mode by both experimental and numerical means. The pertinent experimental work was done by Trinh & Wang (1982) who used an acoustic levitation technique to simulate zero gravity. Numerical work was done by a marker-and-cell method by Foote (1973) and by Alonzo (1974). More recently Benner (1983) used a finite-element computation to further confirm this result. Benner reported some computations at fairly large amplitude. At present there is no large-amplitude theory of drop oscillations.

Our computations will emphasize oscillations of higher modes. We shall compare our results with the fourth-mode analysis of Tsamopoulos & Brown (1983) and with an interesting coupling between the fifth mode and the eighth mode which has been studied by Natarajan & Brown (1986) by a second-order nonlinear analysis. No other direct comparisons for this work have been reported.

The numerical method to be employed is a boundary-integral technique or 'generalized vortex method' in which information known on the free surface alone is used to determine its motion, thus decreasing the dimension of the problem by one. This method has been used by Longuet-Higgins & Cokelet (1976) and by Baker, Meiron & Orszag (1982) to study the breaking of water waves. (References to the work of Baker, Meiron & Orszag will be referred to as BMO.) It has been applied to the nonlinear Rayleigh–Taylor instability by BMO (1980) and to axially symmetric free-surface problems by BMO (1984). Pullin (1982) included surface tension in a study of the Rayleigh–Taylor and Kelvin–Helmholtz instabilities.

We use the boundary-integral method in the dipole representation form developed by BMO. Their formulation is attractive because it results in a Fredholm integral equation of the second kind which may be solved efficiently by an iterative process. This formulation is described in §2 and some preliminary computations are presented in §3.

In the present work the boundary-integral method is applied to the axially symmetric motion of a liquid drop in dynamically inactive surroundings such as a vacuum or low-density gas. Surface tension is essential to the problem and weak viscous effects are accounted for by a new method. The effect of small viscosity can be incorporated into free-surface problems because the primary effects are confined to thin weak vortical surface layers, which in turn require an irrotational correction to the interior flow. By partially solving the appropriate boundary-layer equations analytically, the small viscous change in the potential flow may be calculated by modifying the boundary conditions at the surface. Thus viscous effects are accounted for by the novel means of modifying the pressure boundary condition at the free surface. This idea is developed in §4 and long computations showing the effect of viscosity on some nonlinear oscillations are presented in §5. This method of including viscosity can also be applied to deep-water waves and to fully three-dimensional drop configurations. These more general applications will be dealt with in a separate publication.

The boundary-integral method could be applied equally well to a drop of one liquid surrounded by another of comparable density. Problems of this kind are also of interest in a zero-gravity or simulated zero-gravity environment. Saffren, Elleman & Rhim (1981) have studied oscillations of two-fluid compound drops by the classical Plateau method in which a drop is suspended in a third 'host' liquid of the same density. Experiments simulating zero gravity have been carried out by Trinh & Wang (1982) and Trinh, Zwern & Wang (1982) by acoustically levitating a heavier drop in another liquid. However the effect of viscosity at the interface is much greater in these two-fluid problems (Miller & Scriven 1968) and cannot be accounted for by the method developed in §4. For this reason we have restricted this study to a simple liquid drop in a dynamically inactive environment without any solid boundaries.

2. Basic integral formulation

The motion of a drop of inviscid liquid in a vacuum, or in a gas of negligible density, may be computed by a generalized vortex method described and developed in a series of papers by BMO (1980, 1982, 1984). The method, which is a boundary-integral method, has the advantage of requiring a numerical grid only on the surface of the drop, thus reducing the dimension of the problem by one. In their formulation the velocity potential of an irrotational flow is expressed as a surface distribution of dipoles,

$$\phi(\boldsymbol{r}) = \int_S \mu' \frac{\partial g(\boldsymbol{r},\boldsymbol{r}')}{\partial n'} \mathrm{d}S', \tag{2.1}$$

where

$$g(\boldsymbol{r},\boldsymbol{r}') = -\frac{1}{4\pi|\boldsymbol{r}-\boldsymbol{r}'|}$$

is the velocity potential at a point $\boldsymbol{r}$ due to a unit source at $\boldsymbol{r}'$, a point on the surface S of the drop, $\partial/\partial n'$ is the derivative in the direction of the outer normal to the surface at $\boldsymbol{r}'$ and $\mu' = \mu(\boldsymbol{r}')$ is the dipole density per unit area.

The potential (2.1) is discontinuous across the surface. As $\boldsymbol{r}$ tends to a point on the surface from inside the drop

$$\phi(\boldsymbol{r}) \rightarrow \phi_1 = +\tfrac{1}{2}\mu(\boldsymbol{r}) + \text{P.V.} \int_S \mu' \frac{\partial g(\boldsymbol{r},\boldsymbol{r}')}{\partial n'} \mathrm{d}S', \tag{2.2}$$

while as $\boldsymbol{r}$ tends to the same point from the outside

$$\phi(\boldsymbol{r}) \rightarrow \phi_2 = -\tfrac{1}{2}\mu(\boldsymbol{r}) + \text{P.V.} \int_S \mu' \frac{\partial g(\boldsymbol{r},\boldsymbol{r}')}{\partial n'} \mathrm{d}S', \tag{2.3}$$

where P.V. denotes the principal-value integral. From these results one sees that the dipole density equals the jump in potential across the surface: $\mu = \phi_1 - \phi_2$. Since the normal derivative of ϕ is continuous across the surface (Kellogg 1953), the normal component of the velocity is continuous and therefore (2.1) represents a physically acceptable representation of a flow that is irrotational everywhere except at the surface. Since ϕ itself is discontinuous, the tangential components of the velocity must also be discontinuous and therefore a surface distribution of dipoles is equivalent to a vortex sheet.

In addition to determining the velocity from the gradient of a potential, one can also do this by using the 'generalized Biot–Savart' law. The surface gradient of μ,

$$\nabla_S \mu = \boldsymbol{u}_1 - \boldsymbol{u}_2, \tag{2.4}$$

is a vector which is tangential to the surface. This is related to the circulation density γ of the vortex sheet by

$$\gamma = -\hat{\boldsymbol{n}} \times \nabla_S \mu. \tag{2.5}$$

By introducing a vector potential $\boldsymbol{A}$ with the property

$$\boldsymbol{u} = \nabla \times \boldsymbol{A} \tag{2.6}$$

one can express the vector potential in terms of the vorticity of the flow (Batchelor 1967), which is concentrated at the surface, in the form

$$\boldsymbol{A} = -\int_S \boldsymbol{\gamma}' g(\boldsymbol{r}, \boldsymbol{r}')\,\mathrm{d}S'. \tag{2.7}$$

The usual form of the generalized Biot–Savart law is then obtained by using (2.6), taking the derivative inside the integral. However, by using (2.5) and 'integrating by parts', making use of surface derivative manipulations given in Weatherburn (1927), (2.7) may be written

$$\boldsymbol{A} = -\mathrm{P.V.}\int_S \mu' \hat{\boldsymbol{n}}' \times \boldsymbol{\nabla}'_s g(\boldsymbol{r}, \boldsymbol{r}')\,\mathrm{d}S' \tag{2.8}$$

when $\boldsymbol{r}$ is a point on the surface. The above integral is used to compute $\boldsymbol{A}$ on the surface; then the normal component of the velocity on the surface is obtained from

$$\boldsymbol{u}\cdot\hat{\boldsymbol{n}} = \hat{\boldsymbol{n}}\cdot\boldsymbol{\nabla}\times\boldsymbol{A} \equiv (\hat{\boldsymbol{n}}\times\boldsymbol{\nabla})\cdot\boldsymbol{A}, \tag{2.9}$$

which requires only derivatives of $\boldsymbol{A}$ along the surface. The tangential components of the velocity, on either side of the surface, are obtained by differentiating (2.2) or (2.3) along the surface. Therefore the velocity at the surface can be determined from the dipole density on the surface.

Since the velocity of the surface can be computed, the surface can be evolved in time. Only the normal component of the velocity is required for this since the computed points can be allowed to slide along the surface arbitrarily without affecting the shape. However it seems natural for the present problem to associate the surface with the fluid inside the drop and to allow the computed point to move with the velocity of the fluid by means of

$$\frac{\mathrm{d}\boldsymbol{r}}{\mathrm{d}t} = \boldsymbol{u}_1(\boldsymbol{r}, t), \tag{2.10}$$

where $\boldsymbol{u}_1\cdot\hat{\boldsymbol{n}}$ is computed from (2.9) and $\boldsymbol{u}_1\cdot\hat{\boldsymbol{t}}$ from (2.2). It is worth mentioning that even though the density of the fluid outside the drop is negligible it is still possible to define a velocity there. The surface could be tracked by using the velocity just outside the drop or a weighted average of the velocities inside and outside, as done by BMO (1982).

The additional condition required to determine the dipole density is provided by the pressure boundary condition. That is, the pressure difference across the interface must be balanced by surface tension. Since the outside pressure is zero this condition is

$$p_1 = T\,\mathrm{div}\,\hat{\boldsymbol{n}}, \tag{2.11}$$

where p_1 is the pressure on the fluid side, T is the surface-tension force per unit length, $\hat{\boldsymbol{n}}$ is the outward unit normal and $\mathrm{div}\,\hat{\boldsymbol{n}}$ is the mean curvature expressed as a surface divergence (Weatherburn 1927).

The pressure can be determined from Bernoulli's equation

$$\frac{\partial\phi}{\partial t} + \frac{\boldsymbol{u}\cdot\boldsymbol{u}}{2} + \frac{p}{\rho} = 0, \tag{2.12}$$

which is more conveniently written in terms of the material derivative

$$\frac{\mathrm{d}\phi}{\mathrm{d}t} = \frac{\partial\phi}{\partial t} + \boldsymbol{u}\cdot\boldsymbol{\nabla}\phi = \frac{\partial\phi}{\partial t} + \boldsymbol{u}\cdot\boldsymbol{u} \tag{2.13}$$

as

$$\frac{d\phi}{dt}-\frac{\boldsymbol{u}\cdot\boldsymbol{u}}{2}+\frac{p}{\rho}=0. \tag{2.14}$$

Then, using (2.11),

$$\frac{d\phi_1}{dt}=\frac{\boldsymbol{u}_1\cdot\boldsymbol{u}_1}{2}-\frac{T}{\rho}\operatorname{div}\hat{\boldsymbol{n}}. \tag{2.15}$$

The potential ϕ_1 is related to μ by (2.2) which is an integral equation for μ if ϕ_1 is known. It was pointed out by BMO (1980) that this Fredholm equation of the second kind may be solved by iteration. This is important in order to maintain the advantages of reducing the dimension of the problem by using this boundary-integral method.

To solve for the shape of the drop one must solve (2.10) and (2.15) simultaneously. Given ϕ_1 and the shape of the drop at the beginning of a time step one solves (2.2) for μ. Using μ one computes the vector potential on the surface and hence the normal component of the velocity from (2.9). The tangential components of velocity are then determined by differentiating ϕ_1 along the surface. Hence $\boldsymbol{u}_1$ may be computed at each nodal point on the surface and therefore the right-hand sides of both (2.10) and (2.15) may be computed at each point. The differential equations are then used to get new nodal positions and new ϕ_1 values a short time later.

This strategy is a little simpler than the one used by BMO (1980). Instead of updating ϕ_1 directly, they differentiate the equivalent of (2.2) with respect to time, generating an integral equation for $d\mu/dt$. This requires properly differentiating the integral, accounting for the fact that the interface shape depends on time. The resulting integral equation is the same as (2.2) except for the non-homogeneous term. This is solved for $d\mu/dt$ which is then used to update μ.

The principal-value integrals for $\boldsymbol{A}$ and ϕ_1 may be 'desingularized' by using the known principal-value integrals (Jaswon & Symm 1977)

$$\text{P.V.}\int_S \frac{\partial g(\boldsymbol{r},\boldsymbol{r}')}{\partial n'}\,dS'=\tfrac{1}{2}, \tag{2.16}$$

$$\text{P.V.}\int_S \hat{\boldsymbol{n}}'\times\boldsymbol{\nabla}'_s g(\boldsymbol{r},\boldsymbol{r}')\,dS'=0 \tag{2.17}$$

Thus (2.2) may be written

$$\phi_1=\mu+\int_S(\mu'-\mu)\frac{\partial g(\boldsymbol{r},\boldsymbol{r}')}{\partial n'}\,dS', \tag{2.18}$$

and (2.8) may be written

$$\boldsymbol{A}=-\int_S(\mu'-\mu)\,\hat{\boldsymbol{n}}\times\boldsymbol{\nabla}'_s g(\boldsymbol{r},\boldsymbol{r}')\,dS'. \tag{2.19}$$

The availability of (2.17) to desingularize (2.8) in this way is the chief reason for using (2.8) instead of the more usual form of the Biot–Savart integral.

The equations have been put in dimensionless form throughout the remainder of this paper by using a characteristic length l_0, velocity v_0 and time l_0/v_0. The equations then have identical form, except in (2.15), where T/ρ is replaced by the dimensionless combination $T'=T/\rho v_0^2 l_0$. The length l_0 was taken as a characteristic radius of the drop and T' was set equal to $\frac{1}{2}$, making $v_0=(2T/\rho l_0)^{\frac{1}{2}}$.

While the formulation has described arbitrary three-dimensional drops, computations have not yet reached this level of generality. All of the computations to be presented here are restricted to axially symmetric shapes such as that shown in figure 1, where a consistent cylindrical coordinate system is depicted. Here z and r are axial

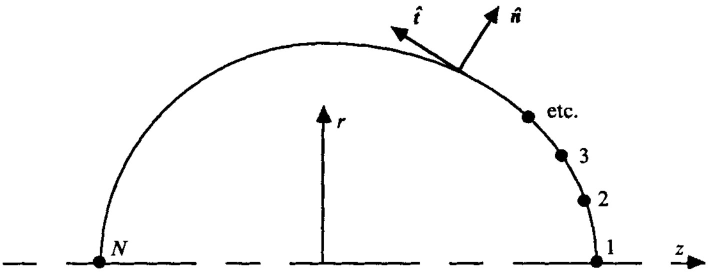

FIGURE 1. Axially symmetric coordinate system.

and radial variables, s is arclength along the intersection of a meridian plane with the drop, measured from the right-hand end as indicated. $\hat{n}(s)$ and $\hat{t}(s)$ are local normal and tangent vectors. The normal to the meridian plane $\hat{\theta}$ is directed out of the page.

For axially symmetric drops the vector potential only has a component in the $\hat{\theta}$-direction, $A = A_\theta \hat{\theta}$, and the normal and tangential velocity components are given by

$$u_1 \cdot \hat{n} = r^{-1} \frac{\partial r A_\theta}{\partial s} \tag{2.20}$$

and

$$u_1 \cdot \hat{t} = \frac{\partial \phi_1}{\partial s}. \tag{2.21}$$

In the surface integrals defining A and ϕ_1 the integrations over the angular variable may be carried out, giving line integrals of the form

$$A_\theta = -\int (\mu(s') - \mu(s)) K_A(s, s') \, ds', \tag{2.22}$$

$$\phi_1 = \mu + \int (\mu(s') - \mu(s)) K_\phi(s, s') \, ds' \tag{2.23}$$

where the kernels K_A and K_ϕ are complicated singular functions that depend on elliptic integrals. These were computed using the accurate approximation formulae given in Abramowitz & Stegun (1972). Nodes were numbered from 1 to N with 1 at the right end and N at the left. A Lagrangian integration variable ξ was introduced with fixed identity at each of the nodes. It was convenient to let ξ vary from 1 to N, taking the value j at the jth node. A change of variables from s' to ξ' puts the integrals in the form

$$A_\theta = -\int_1^N (\mu(\xi') - \mu(\xi)) K_A(\xi, \xi') \lambda' \, d\xi', \tag{2.24}$$

where

$$\lambda = \frac{\partial s}{\partial \xi} = \left(\left(\frac{\partial z}{\partial \xi}\right)^2 + \left(\frac{\partial r}{\partial \xi}\right)^2\right)^{\frac{1}{2}} \tag{2.25}$$

cancels out of the integrands because the kernels are linear in the components of the tangent vector, i.e. $t_z = \partial z/\partial s = \lambda^{-1} \partial z/\partial \xi$. Quantities like $\partial z/\partial \xi$ and $\partial r/\partial \xi$ were computed at the nodes from the nodal values of z and r by using a fourth-order-accurate Padé approximate difference formula. The nodes were equally spaced in the ξ-variable. It was not necessary to calculate the physical distance between nodes along the curve except for plotting purposes.

Because the elliptic integrals are more rapidly varying between the nodes, especially near the poles, it was necessary (following the suggestion of BMO 1984) to insert additional points between the nodal points. Therefore it was necessary to interpolate for the values of z, r, and μ at the inserted points. Since the derivatives of these quantities are already known at the nodes an interpolation formula was used that fits a cubic polynomial in ξ to the values of these functions and their derivatives at the end points of a nodal interval. This interpolation is fourth-order accurate. The integrals were then approximated by using the midpoint formula between the equally spaced inserted points.

The integrals are thus evaluated as functions of the coordinate positions of the nodes and the values of μ at the nodes. The velocities at the nodes are then obtained from (2.20) and (2.21) using the Padé approximate first-derivative formula. The surface-tension term requires second derivatives of the coordinate positions. These were evaluated using a fourth-order-accurate Padé approximate second-derivative formula. Finally values of z, r and ϕ_1 at the nodes were updated by using (2.10) and (2.15) with fourth-order Runge–Kutta time advancement. It usually required about ten iterations to obtain μ to an accuracy of 10^{-5}.

We observe a loss of accuracy of the velocity computation near the poles, but this is not as severe a loss as that reported by de Bernadinis & Moore (1985) who used the Van der Vooren approach to desingularize Biot–Savart integrals. We repeated their test computation with the known solution for the surface velocity of a suddenly accelerated sphere. For the same number of nodes our computation, with four added integration points between nodes, is not as accurate as theirs (for this test problem) because we start with the known dipole strength, do an integration and then differentiate to get the velocity, whereas they start with the known circulation density and do not have a differentiation after the integration. With 100 nodes their accuracy deteriorates rapidly from about 10^{-7} to 10^{-4} near the poles, while ours varies from about 10^{-5} to 10^{-4}. Despite the extra differentiation, our accuracy near the poles is the same as theirs. That is, our *loss* of accuracy near the poles is not as extreme. Further, as the number of added points between nodes is increased, the loss of accuracy near the poles decreases. We conclude that the loss of accuracy is caused by the rapid variation of the elliptic integrals between nodes near the poles.

It often happens that after a number of time steps the nodes become bunched together over part of the drop. This can lead to numerical instabilities (the closer spacing requires a smaller time step to keep the fourth-order Runge–Kutta algorithm stable) and has been prevented by remeshing the nodes so that they are approximately evenly spaced. The required interpolation for new nodal positions and μ-values (and interpolated values of $\partial z/\partial \xi$ and $\partial y/\partial \xi$) was accomplished by using cubic splines. Remeshing was normally done after every time step.

The local energy and volume were monitored to keep track of overall accuracy. The kinetic energy was computed from the classical formula (Lamb 1932, §44)

$$E_{\mathrm{K}} = \frac{\text{Kinetic Energy}}{\frac{1}{2}\rho v_0^2 l_0^3} = \int_S \hat{\boldsymbol{n}}\cdot\boldsymbol{u}\,\phi_1\,\mathrm{d}S, \tag{2.26}$$

and the surface energy from

$$E_{\mathrm{P}} = \frac{\text{Surface Energy}}{\frac{1}{2}\rho v_0^2 l_0^3} = 2T'S, \tag{2.27}$$

where S is the surface area and $T'(=\frac{1}{2})$ is the dimensionless surface tension introduced earlier.

3. Preliminary computations: instabilities

We have done test computations with two kinds of single-mode initial conditions: the Rayleigh shape initial condition

$$r = 1+\epsilon_n P_n(\cos\Theta), \quad \phi = 0; \tag{3.1}$$

or the impulsive initial condition

$$r = 1, \quad \phi = \phi_n P_n(\cos\Theta), \tag{3.2}$$

which can be thought of as applying an impulsive pressure at the initial time. The parameter ϵ_n is the initial axial displacement of the pole ends of the drop, a quantity that we refer to as amplitude. We have done computations with moderate to large values of ϵ_n or ϕ_n where mode coupling will occur. For small ϵ_n or ϕ_n with n not too large the computed solutions were found to consist of sinusoidal oscillations of the Legendre-polynomial mode shape as expected. However for larger amplitudes instabilities developed. For example with initial conditions $r = 1, \phi = 0.6P_2$ exponentially growing waves of a zigzag mode with wavelength twice the nodal spacing (2Δ waves) as shown in figure 2(*a*) appear after a relatively short time. The quantity shown is the circulation density (the negative of the derivative of the dipole density, i.e. the difference in velocity) along the drop surface. Growing waves also appear on the surface, but they are always much less evident than these. Similar instabilities have been reported by Longuet-Higgins & Cokelet (1976), BMO (1982) and by Pullin (1982).

Moore (1982) analysed the instabilities for two-dimensional interfacial waves and concluded that with his numerical scheme the system is linearly stable, the instability being caused by a nonlinear interaction between modes. These appeared to be a threshold amplitude below which the system was stable. The modal frequencies at first increased with mode number following the linear theory then, distorted by the numerical scheme, decreased to zero at a mode number equal to the number of nodes, presenting the possibility of resonance between the high modes and the low modes.

The present system with surface tension and axial symmetry and some algorithm difference behaves in a different manner. A number of low-amplitude single-mode computations with initial conditions given by (3.1) have been made with $N = 101$. The mode P_n has n zero crossings and $\frac{1}{2}n$ waves between the poles. Thus P_{100} has 50 waves and represents 2Δ waves. We find that the modal frequency increases monotonically with n, levelling off at the highest mode number, 100. This difference from Moore's observation is probably due to surface tension. The 2Δ and 3Δ waves are unstable when directly excited through P_{100} and P_{66} at any amplitude. Because of the small number of nodes available per wave these short-wave modes appear about the same, with the same period (about 0.02), growth rate (about 25% per cycle) and the same characteristic unstable mode shape. The latter, shown in figure 2(*b*), looks similar to the instability shown in figure 2(*a*) with mostly 2Δ and 3Δ zigzags and much higher amplitude near the poles. (High-order Legendre polynomials are much larger near the poles, by a factor of 12 for P_{100}). These may be the same unstable mode since it is probably impossible to isolate a stable 3Δ wave without strongly exciting the 2Δ instability. The 4Δ wave excited by P_{50} is also unstable with period 0.025 and growth rate about 7% per cycle. The growing mode looks like the function P_{50} with 25 irregular 4Δ zigzag waves. After about 10 cycles faster growing 2Δ zigzags show up near the poles.

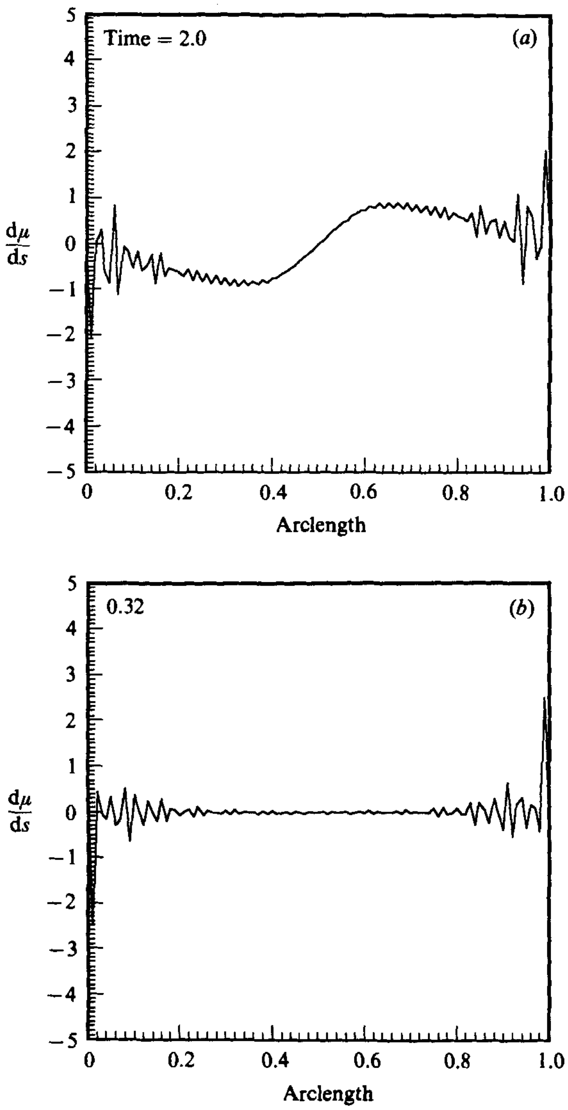

FIGURE 2. Circulation density showing 2Δ instability: (*a*) as it appears on a second-mode oscillation, (*b*) generated by P_{100}.

Typical of lower modes, P_{25} appears to be stable for 10 or 12 cycles but then becomes unstable when the higher frequency unstable mode described above becomes apparent. There is no threshold amplitude. Nearly identical results occur for initial amplitudes of 10^{-4}, 10^{-5}, and 10^{-6}. In this case it appears that the unstable zigzag mode was present at low amplitude in the initial discretization, in the same proportion relative to the initial amplitude, and only became evident when it had outgrown the amplitude of the stable 25th mode.

These computations with the 25th mode were done with a time step $\Delta t = 0.002$. As we increase Δt we find *stability* in the range $0.004 > \Delta t > 0.0085$. This is a consequence of the favourable stabilizing effect of the fourth-order Runge–Kutta time-stepping algorithm which is able to compensate for the 25% per cycle growth rate of the zigzag mode in this range.

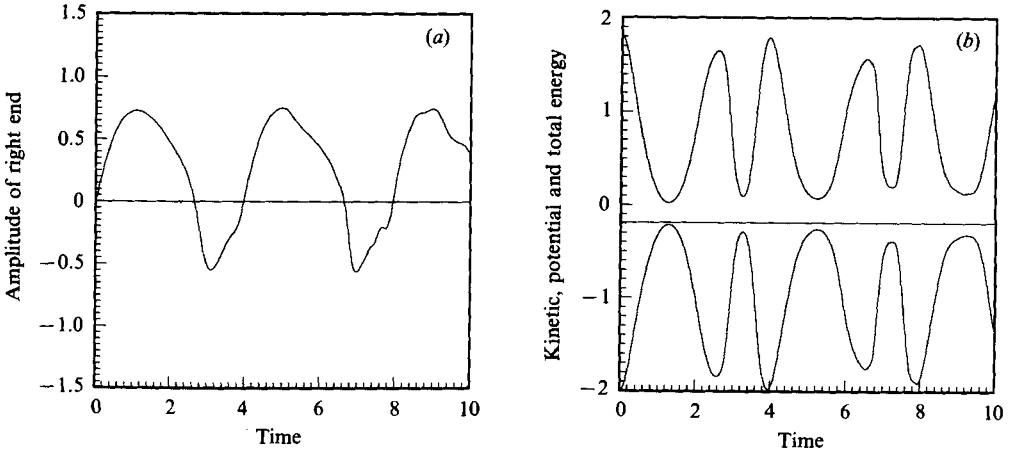

FIGURE 3. Second-mode oscillations with initial conditions. $\phi = 0.6P_2, r = 1$; $N = 101$, $\Delta t = 0.005$, $D_1 = 0.01$. (a) Amplitude of right-hand polar point, $z(1)-z_0(1)$. (b) Energy. The upper oscillatory trace is the kinetic energy, the lower oscillatory trace is potential energy (surface energy) with arbitrarily shifted ordinate. The straight line is the total energy.

We conclude that there is an accuracy problem. Except in the narrow stable window the instability will always be seen eventually because of initial error or round-off error. It can also occur because of nonlinear transfer of energy to higher modes, not by direct resonance with a lower mode but perhaps by other combinations of mode coupling. However, the basic cause of the instability is still not known.

To combat this problem Longuet-Higgins & Cokelet (1976) used five-point numerical smoothing of the interface shape. Dommermuth & Yue (1987), using an integral formulation similar to that of Longuet-Higgins & Cokelet have found stability by remeshing alone. BMO (1982) solved this problem by improving the accuracy of their algorithms and limiting the length of their computations. Pullin (1982) has smoothed both the surface shape and the surface potential. Kraszny (1986) has used a form of smoothing that involves a new filtering technique. We have smoothed in the following manner. In addition to remeshing, which is a form of smoothing, we have directly smoothed the surface potential after each time step by using one smoothing step derived from

$$\frac{\partial \phi}{\partial t} = -\lambda \frac{\partial^4 \phi}{\partial \xi^4} \tag{3.3}$$

using a five-point formula for the fourth derivative and an Euler time step. This has the same effect as placing the fourth derivative on the right-hand side of (2.15) and causes damping of the higher modes while having a minimal effect on the lower modes. Specifically, we smoothed by replacing the values of the potential, ϕ_j, by

$$\phi_j + D_1(\phi_{j+2} - 4\phi_{j+1} + 6\phi_j - 4\phi_{j-1} + \phi_{j-2}). \tag{3.4}$$

When applied to the 25th-mode test case, with an appropriate value of the smoothing parameter $D_1 = 0.01$, the stable window is enlarged to $0 < \Delta t < 0.085$. There is not much change in the upper limit because it was already very close to the Runge–Kutta stability limit.

The nonlinear case attempted above ($r = 1, \phi_2 = 0.6P_2$) was rerun with $D_1 = 0.01$ and $N = 101$ with the results shown in figure 3 (*a*, *b*). This case was chosen to compare with one computed by Benner (1983) by a finite-element method and appears to give identical results. (In our units the time is half of Benner's and the potential is double.) The lower curve in figure 3 (*b*) is the potential energy. It has been arbitrarily shifted so that it starts from -2. The total energy (the straight line) is the sum of the kinetic energy and the shifted potential energy. The energy loss due to smoothing is 0.0024 compared to the maximum kinetic energy of 1.8 or about 0.05% loss per cycle. This same case was run with $N = 61$, with 0.15% loss per cycle but otherwise identical results. It is of interest that this test case with $N = 101$ and no smoothing runs stably with $\Delta t = 0.0065$ and $\Delta t = 0.0075$ which are within the stable window established for the 25th-mode linear calculations. In these cases the energy error was less than 10^{-4}. While it would be desirable to eliminate the need for smoothing by operating in the stable window it is often necessary to have Δt smaller than the allowed values for accuracy.

More extreme examples of this type have been computed to show the possibilities of this method. Initial conditions were chosen as $r = 1, \phi = \phi_2 P_2$ with larger values of ϕ_2. This initial condition can be thought of as an impulsive pressure applied initially in such a way as to drive the poles of the drop in opposite directions. This could be approximated experimentally by applying a large axial electric field to a conducting drop for a short time. With a large impulse the drop becomes very elongated and breaks into several pieces. In figure 4 several views of this process are shown, together with the circulation density along the surface starting from the right-hand end and following along the upper half-meridian plane. Figure 4 (*a*) shows a sequence with the carefully selected value $\phi_2 = 0.86$ for which the drop will break in half. The first view shows the drop near full extension and the last just before the computation fails when the throat contracts to zero. (This computation could be continued by reconnecting the ends as was done by Fromm 1984 in the pinch-off of a drop-on-demand jet.) As the droplet begins to pinch off, strong spikes of vorticity develop at each side of the throat consistent with the observed steepening of the attachment between the throat and the droplet where the curvature becomes large. The sign of the vorticity (because of the way it is plotted, the positive spike is on the right-hand droplet) would cause these vortex rings to move away from each other in the absence of other induced-velocity contributions from more distant vorticity. These local induced velocities are such as to remove fluid from the throat. We cannot tell whether the drops would actually separate after pinch-off since the ends of the drop actually appear to be moving toward each other. When ϕ_2 is slightly smaller than 0.86 (we have computed with 0.85) the throat rebounds and the drop oscillates. When ϕ_2 is slightly greater than 0.86 (we have used values as close as 0.87) the drop appears to break into three parts with a very small central satellite. As ϕ_2 continues to increase the satellite increases in size until it becomes the dominant part. Figure 4 (*b*) shows a sequence for $\phi_2 = 1.0$, and figure 4 (*c*) shows one for $\phi_2 = 1.3$. Notice that the vorticity spikes continue to form on the inner portions of the outer drops, but none appear on the incipient satellite drop. We have computed with ϕ_2 as large as 2.5, in which case the drop becomes stretched to a length-to-width ratio of about 20 before forming relatively small end drops. If these were removed by reconnection, would secondary end drops begin to pinch off?

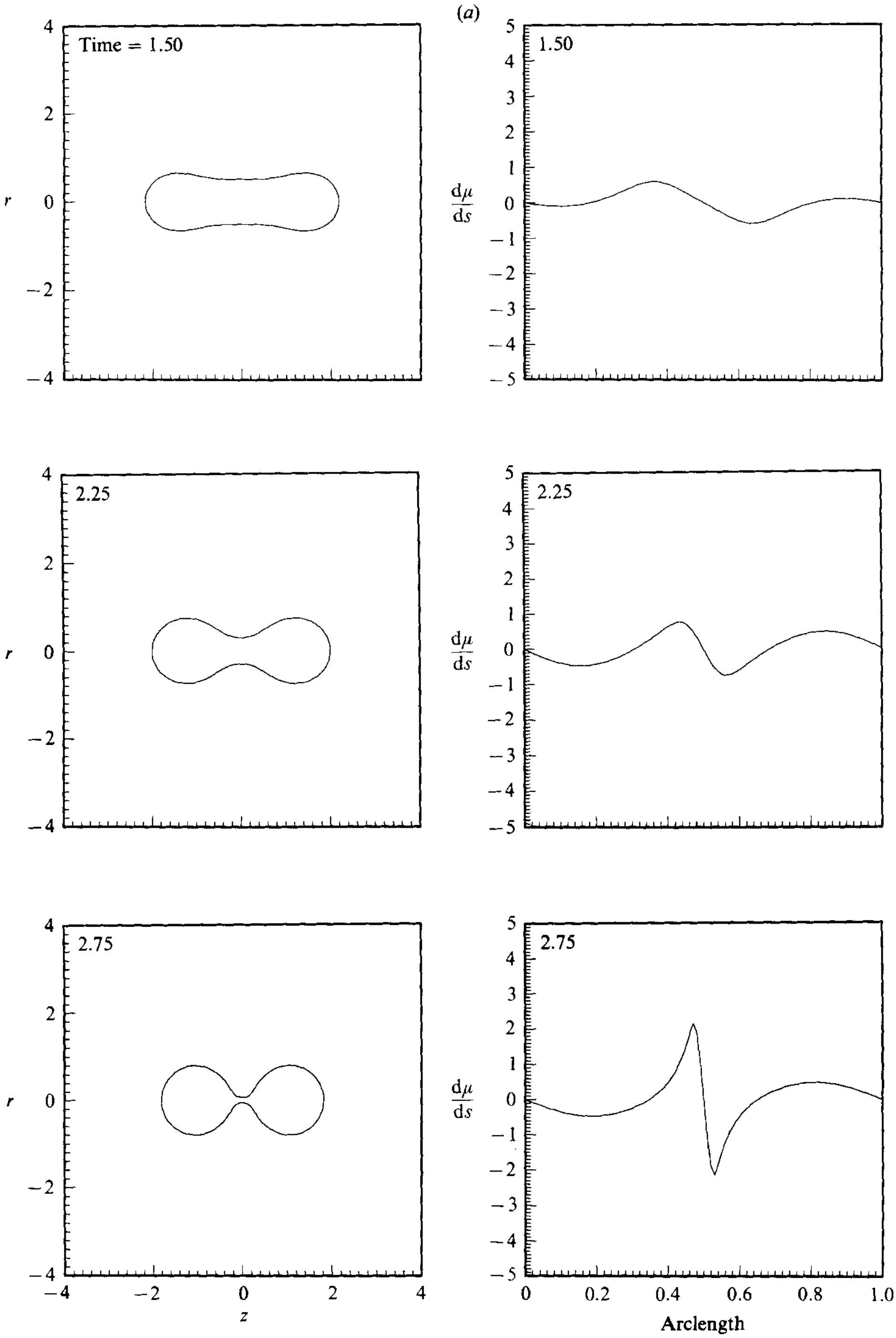

FIGURE 4(*a*). For caption see page 492.

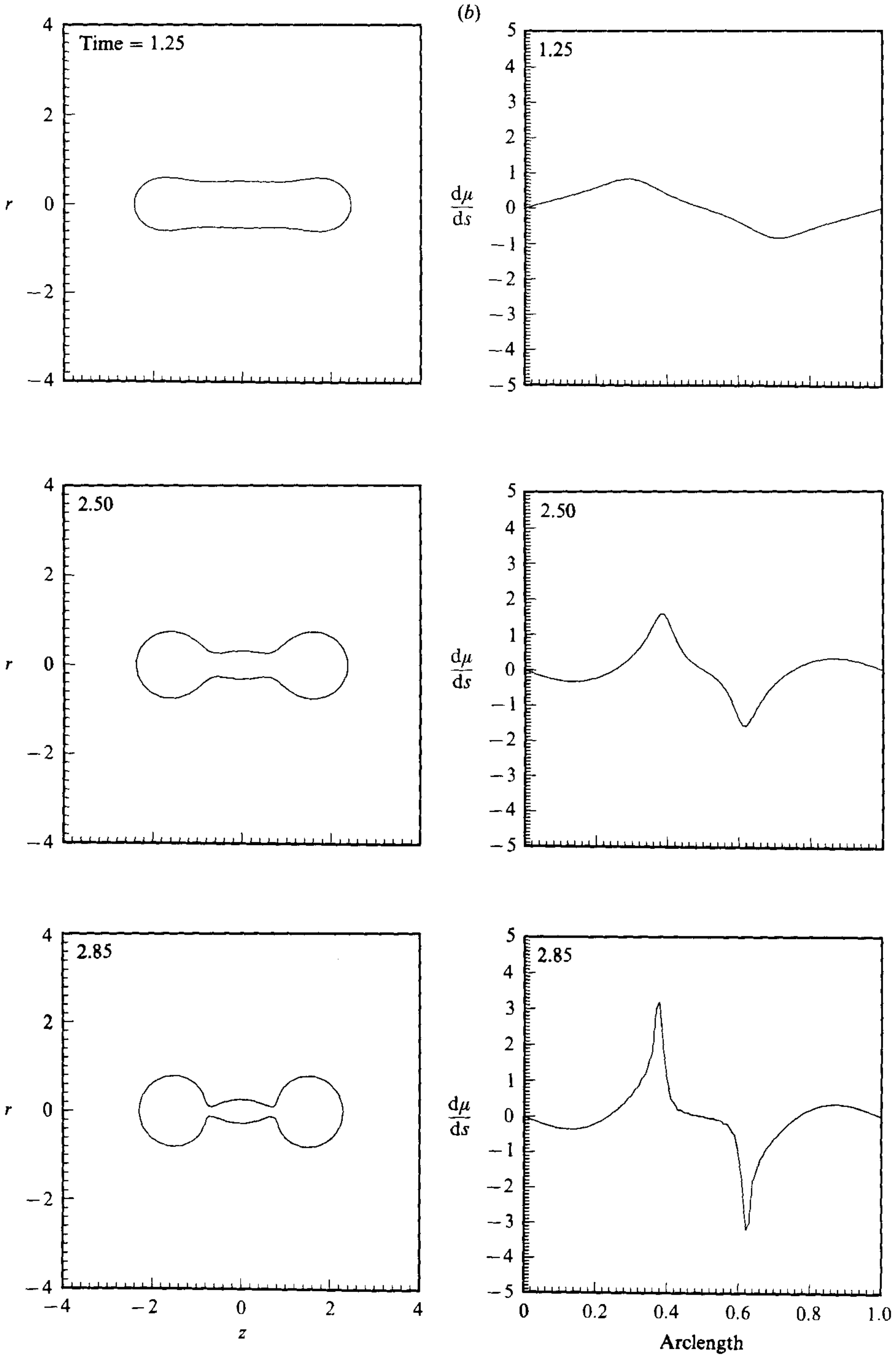

FIGURE 4(*b*). For caption see page 492.

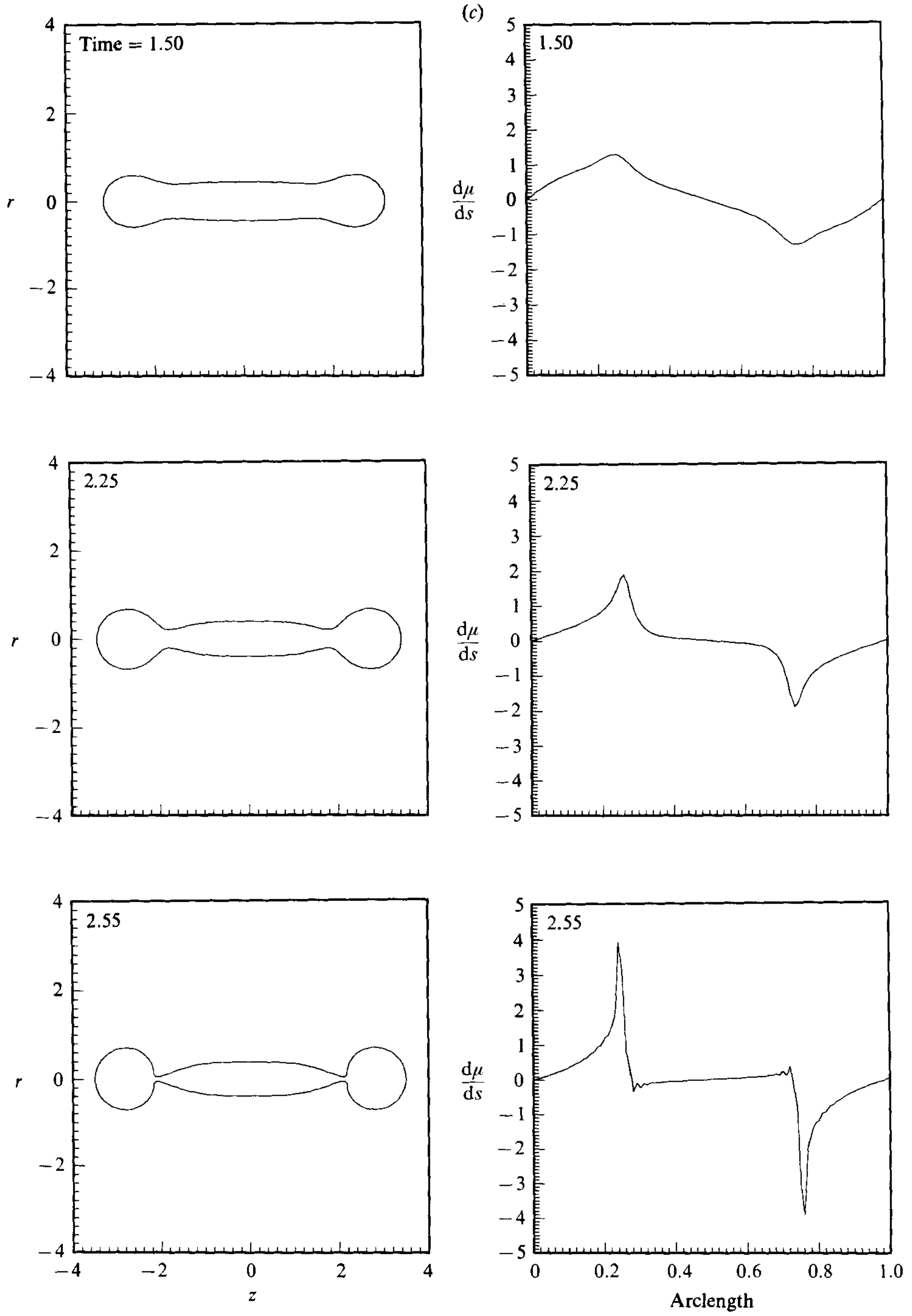

FIGURE 4. Drop breakup from initial impulse. Initial conditions are: (*a*) $\phi = 0.86P_2$; $r = 1$, (*b*) $\phi = 1.0P_2, r = 1$; (*c*) $\phi = 1.3P_2, r = 1$. $N = 101$, $\Delta t = 0.005$, $D_1 = 0.01$. Drop shapes (the left-hand traces) are shown near the state of maximum extension (*a*), just before the computation fails when the droplet throats pinch to zero (*c*), and at an intermediate time (*b*). The right-hand traces are the circulation density versus normalized arclength along the drop surface measured from the right-hand end of the drop. When the parameter is smaller than 0.86 the drop oscillates. When it is greater than this value a satellite drop forms.

4. Weak viscous effects

The method developed in §2 is based on inviscid analysis and cannot be used to study the damping effects of viscosity on drop oscillations. In this section a new method is presented which introduces high-Reynolds-number viscous effects by modifying the boundary conditions at the free surface. It turns out that the viscous effects are not always strong enough to damp the instabilities and, in fact, sometimes trigger the instability, so smoothing must still be used.

Lamb (1932, §349) presents a linearized theory for viscous damping of deep-water waves. He shows that viscosity produces a thin, weak vortical layer at the free surface. This is distinct from the potential vortex sheet, which remains sharp, and is not the same as a diffusive thickening of the vortex sheet. The vortical layer occurs because the irrotational shear stress is not zero at the free surface (unless the viscosity is identically zero). This small irrotational shear stress drags a thin viscous layer of rotational fluid along, making the small modification to the velocity field that is required in order to satisfy the zero-shear-stress boundary condition. A key point which makes the analysis below possible is that the vorticity at the free surface is completely determined by the irrotational part of the shear stress. This vortical layer is thin. The flow remains irrotational (even though affected by viscosity) throughout the bulk of the fluid. Lamb (1932) and Batchelor (1967) point out that the dissipation is mainly in the irrotational part of the flow, not in the vortical layer as would be the case at a solid boundary or at an interface between two immiscible liquids with comparable viscosities. Moore (1962) used some of these ideas in studying the boundary layer on the outside of a spherical gas bubble. Miksis, Vanden-Broek & Keller (1982) applied them to the flow around a non-spherical bubble neglecting the vortical layer and the pressure drop across it in the normal stress boundary condition. In general this pressure correction is comparable to the normal stress viscous correction (which can be computed from the potential flow), but this was less important in their particular problem. Hasegawa & Yamashita (1986), following Miksis *et al.*, made the same approximation in a different kind of problem where the neglected pressure drop is probably important.

In this section a nonlinear version of these results will be presented for axially symmetric flow. By solving for the vortical layer enough information can be found to include weak viscous effects as a boundary condition at the free surface of an otherwise irotational flow.

Consider an incompressible fluid with a free surface which separates it from a vacuum (or dynamically inactive fluid). The fluid velocity V must satisfy

$$\nabla \cdot V = 0, \tag{4.1}$$

$$\frac{\partial V}{\partial t} + V \cdot \nabla v = -\nabla p + R_e^{-1} \nabla^2 V. \tag{4.2}$$

The Navier–Stokes equations are written here in the dimensionless form introduced in §2 in which the scaling is such that p is the pressure divided by ρv_0^2 and $R_e = l_0 v_0/\nu$ is a Reynolds number. As a point of reference a drop of water in air with radius 2 cm has $R_e = 2400$ in our units.

For axially symmetric flow V lies in a meridian plane. The boundary conditions at the free surface are then:

(i) shear stress is zero:

$$\hat{\boldsymbol{t}} \cdot \boldsymbol{T} \cdot \hat{\boldsymbol{n}} \equiv 2R_e^{-1}\, \hat{\boldsymbol{t}} \cdot \boldsymbol{D} \cdot \hat{\boldsymbol{n}} = 0, \tag{4.3}$$

where $\boldsymbol{D}$ is the rate-of-strain tensor with Cartesian components

$$D_{ij} = \tfrac{1}{2}(\partial v_i/x_j + \partial v_j/\partial x_i);$$

(ii) normal stress is balanced by surface tension:

$$\hat{\boldsymbol{n}}\cdot\boldsymbol{T}\cdot\hat{\boldsymbol{n}} \equiv -p+2R_e^{-1}\,\hat{\boldsymbol{n}}\cdot\boldsymbol{D}\cdot\hat{\boldsymbol{n}} = -T'\,\mathrm{div}\,\hat{\boldsymbol{n}} \tag{4.4}$$

where $T'(=\tfrac{1}{2})$ is the dimensionless surface tension introduced before.

Let the velocity field be decomposed into the sum of irrotational and vortical parts, by

$$\boldsymbol{V} = \boldsymbol{u}+\boldsymbol{U}, \tag{4.5}$$

where

$$\boldsymbol{u} = \boldsymbol{\nabla}\phi, \tag{4.6}$$

$$\boldsymbol{U} = \boldsymbol{\nabla}\times\boldsymbol{A}_2, \quad \boldsymbol{\nabla}\cdot\boldsymbol{A}_2 = 0. \tag{4.7}$$

For axially symmetric flow $\boldsymbol{A}_2 = A_2\hat{\boldsymbol{\theta}}$. Since the irrotational part can also be expressed as the curl of a vector potential, it will be assumed for uniqueness that A_2 is zero in the interior part of the flow. Then the irrotational part of the flow will be entirely determined by the potential induced by the vortex sheet. From the continuity equation $\nabla^2\phi = 0$ and by a vector identity the vorticity is given by $\omega = -\nabla^2 A_2$. The scalar A_2 is an axially symmetric stream function. The excess flux (relative to the potential flow) in the layer is $2\pi r A_2$.

Similarly the pressure is decomposed as

$$p = -\frac{\partial\phi}{\partial t}-\frac{\boldsymbol{u}\cdot\boldsymbol{u}}{2}+P, \tag{4.8}$$

where the first two terms on the right give the pressure associated with the irrotational part of the flow, and P is the excess pressure required for the vortical flow. Without loss of generality P may be assumed to be zero in the interior part of the flow. Substituting (4.5) and (4.8) into the Navier–Stokes equations gives

$$\boldsymbol{\nabla}\cdot\boldsymbol{U} = 0, \tag{4.9}$$

$$\frac{\partial\boldsymbol{U}}{\partial t}+\boldsymbol{U}\cdot\boldsymbol{\nabla}\boldsymbol{u}+\boldsymbol{u}\cdot\boldsymbol{\nabla}\boldsymbol{U}+\boldsymbol{U}\cdot\boldsymbol{\nabla}\boldsymbol{U} = -\boldsymbol{\nabla}P+R_e^{-1}\nabla^2\boldsymbol{U}. \tag{4.10}$$

We wish to show, by using standard boundary-layer estimates, that $\boldsymbol{U}$ is small and confined to a thin layer along the surface. Introduce a local orthogonal coordinate system in the surface layer with ζ a coordinate in the direction of $\hat{\boldsymbol{n}}$ (so that ζ is negative in the fluid), s the arclength along the surface in the direction of $\hat{\boldsymbol{t}}$ and with the third coordinate the azimuthal angle.

Decomposing the shear strains into rotational and irrotational parts, and noting that the rate-of-strain tensor for the irrotational part is $\boldsymbol{\nabla}\boldsymbol{u}$, the shear-stress boundary condition becomes

$$\hat{\boldsymbol{t}}\cdot\boldsymbol{\nabla}\boldsymbol{u}\cdot\hat{\boldsymbol{n}}+\tfrac{1}{2}(\hat{\boldsymbol{t}}\cdot\boldsymbol{\nabla}\boldsymbol{U}\cdot\hat{\boldsymbol{n}}+\hat{\boldsymbol{n}}\cdot\boldsymbol{\nabla}\boldsymbol{U}\cdot\hat{\boldsymbol{t}}) = 0. \tag{4.11}$$

Assuming that the vortical layer has thickness of order δ, with $\delta \leqslant 1$, and that the scale of variation along the layer is of order one, the vortical terms in (4.11) can be estimated as

$$\hat{\boldsymbol{t}}\cdot\boldsymbol{\nabla}\boldsymbol{U}\cdot\hat{\boldsymbol{n}}+\hat{\boldsymbol{n}}\cdot\boldsymbol{\nabla}\boldsymbol{U}\cdot\hat{\boldsymbol{t}} \approx \frac{\partial U_t}{\partial\zeta}, \tag{4.12}$$

where $U_t = \boldsymbol{U}\cdot\hat{\boldsymbol{t}}$. So

$$\frac{\partial U_t}{\partial \zeta} \approx -2\hat{\boldsymbol{t}}\cdot\nabla\boldsymbol{u}\cdot\hat{\boldsymbol{n}}. \tag{4.13}$$

Since $\hat{\boldsymbol{t}}\cdot\nabla\boldsymbol{u}\cdot\hat{\boldsymbol{n}}$ is of order one this implies that U_t is of order δ and, from (4.7), $A_2 = O(\delta^2)$. Furthermore, from the continuity equation, $U_n = O(\delta^2)$.

With these estimates of U_t, U_n and $\boldsymbol{u}$, and neglecting some small viscous terms and $\boldsymbol{U}\cdot\nabla\boldsymbol{U}$, which is of order δ^2, (4.10) may be written

$$\frac{\mathrm{D}\boldsymbol{U}}{\mathrm{D}t}+\boldsymbol{U}\cdot\nabla\boldsymbol{u} = -\nabla P + R_e^{-1}\frac{\partial^2 \boldsymbol{U}}{\partial \zeta^2}, \tag{4.14}$$

where $\mathrm{D}/\mathrm{D}t = \partial/\partial t + \boldsymbol{u}\cdot\nabla$ is a temporary notation. The tangential and normal components of this equation are

$$\frac{\mathrm{D}U_t}{\mathrm{D}t} - \boldsymbol{U}\cdot\frac{\mathrm{D}\hat{\boldsymbol{t}}}{\mathrm{D}t} + \boldsymbol{U}\cdot\nabla\boldsymbol{u}\cdot\hat{\boldsymbol{t}} = -\frac{\partial P}{\partial s} + R_e^{-1}\frac{\partial^2 U_t}{\partial \zeta^2} \tag{4.15}$$

and

$$\frac{\mathrm{D}U_n}{\mathrm{D}t} - \boldsymbol{U}\cdot\frac{\mathrm{D}\hat{\boldsymbol{n}}}{\mathrm{D}t} + \boldsymbol{U}\cdot\nabla\boldsymbol{u}\cdot\hat{\boldsymbol{n}} = -\frac{\partial P}{\partial \zeta} + R_e^{-1}\frac{\partial^2 U_n}{\partial \zeta^2}. \tag{4.16}$$

In (4.15), the first term on the left is of order δ, even though the individual terms in this combination are larger than this. It is easy to see that if $\boldsymbol{u}$ has a component perpendicular to the surface then $\boldsymbol{u}\cdot\nabla U_t = O(1)$; however since this combination of terms is a material derivative following the potential flow the rapidly varying spatial variation of U_t must be cancelled by an equally rapid temporal variation. The second term on the left in (4.15) is of order δ^2 as is the part of the third term that depends on U_n. Since the viscous term is of order $(\delta R_e)^{-1}$ it follows that

$$\delta = R_e^{-\frac{1}{2}}, \tag{4.17}$$

as in boundary layers on solid surfaces and in agreement with Lamb and Moore.

Inspection of (4.16) shows that $\partial P/\partial\zeta = O(\delta)$ and, since P is zero in the interior, $P = O(\delta^2)$ in the vortical layer and therefore $\partial P/\partial s$ may be neglected in (4.15), which simplifies to

$$\frac{\mathrm{D}U_t}{\mathrm{D}t} + U_t\,\hat{\boldsymbol{t}}\cdot\nabla\boldsymbol{u}\cdot\hat{\boldsymbol{t}} = R_e^{-1}\frac{\partial^2 U_t}{\partial \zeta^2} + O(\delta^2). \tag{4.18}$$

Using $U_t = -\partial A_2/\partial\zeta$, from (4.7), in (4.18) and the fact that $\boldsymbol{u}$ is slowly varying in the vortical layer, each of the terms may be written as derivatives with respect to ζ, i.e.

$$\left.\begin{aligned}
\boldsymbol{u}\cdot\nabla U_t &= -\boldsymbol{u}\cdot\nabla\frac{\partial A_2}{\partial \zeta},\\
&= -\frac{\partial(\boldsymbol{u}\cdot\nabla A_2)}{\partial \zeta} + \frac{\partial \boldsymbol{u}}{\partial \zeta}\cdot\nabla A_2,\\
&= -\frac{\partial(\boldsymbol{u}\cdot\nabla A_2)}{\partial \zeta} + \hat{\boldsymbol{n}}\cdot\nabla\boldsymbol{u}\cdot\hat{\boldsymbol{n}}\frac{\partial A_2}{\partial \zeta} + O(\delta^2),\\
&= \frac{\partial(-\boldsymbol{u}\cdot\nabla A_2 + \hat{\boldsymbol{n}}\cdot\nabla\boldsymbol{u}\cdot\hat{\boldsymbol{n}}A_2)}{\partial \zeta} + O(\delta^2),
\end{aligned}\right\} \tag{4.19}$$

and

$$\left.\begin{aligned} U_t\,\hat{\boldsymbol{t}}\cdot\boldsymbol{\nabla}\boldsymbol{u}\cdot\hat{\boldsymbol{t}} &= -\hat{\boldsymbol{t}}\cdot\boldsymbol{\nabla}\boldsymbol{u}\cdot\hat{\boldsymbol{t}}\frac{\partial A_2}{\partial\zeta}, \\ &= \frac{\partial(-\hat{\boldsymbol{t}}\cdot\boldsymbol{\nabla}\boldsymbol{u}\cdot\hat{\boldsymbol{t}}A_2)}{\partial\zeta}+O(\delta^2). \end{aligned}\right\} \tag{4.20}$$

Upon using

$$\hat{\boldsymbol{n}}\cdot\boldsymbol{\nabla}\boldsymbol{u}\cdot\hat{\boldsymbol{n}} = -\boldsymbol{t}\cdot\boldsymbol{\nabla}\boldsymbol{u}\cdot\hat{\boldsymbol{t}}-\boldsymbol{u}\cdot\hat{\boldsymbol{r}}/r, \tag{4.21}$$

which follows from div $\boldsymbol{u} = 0$, (4.18) may be written

$$\frac{\partial(\mathrm{D}A_2/\mathrm{D}t+2A_2\,\hat{\boldsymbol{t}}\cdot\boldsymbol{\nabla}\boldsymbol{u}\cdot\hat{\boldsymbol{t}}+\boldsymbol{u}\cdot\hat{\boldsymbol{r}}A_2/r+R_e^{-1}\,\partial U_t/\partial\zeta)}{\partial\zeta} = O(\delta^2). \tag{4.22}$$

Integrating this into the interior where A_2 is zero gives

$$\frac{\mathrm{D}A_2}{\mathrm{D}t} = -(2\hat{\boldsymbol{t}}\cdot\boldsymbol{\nabla}\boldsymbol{u}\cdot\hat{\boldsymbol{t}}+\boldsymbol{u}\cdot\hat{\boldsymbol{r}}/r)\,A_2-R_e^{-1}\frac{\partial U_t}{\partial\zeta}+O(\delta^3). \tag{4.23}$$

If we were to substitute $U_t = -\partial A_2/\partial\zeta$ into the viscous term this would be a partial differential equation for A_2 in the layer. However it is not necessary to solve this, because by evaluating it at the boundary and using the boundary condition (4.13) in place of the viscous term we find

$$\frac{\mathrm{D}A_2}{\mathrm{D}t} = -(2\hat{\boldsymbol{t}}\cdot\boldsymbol{\nabla}\boldsymbol{u}\cdot\hat{\boldsymbol{t}}+\boldsymbol{u}\cdot\hat{\boldsymbol{r}}/r)\,A_2+2R_e^{-1}\,\hat{\boldsymbol{t}}\cdot\boldsymbol{\nabla}\boldsymbol{u}\cdot\hat{\boldsymbol{n}}+O(\delta^3), \tag{4.24}$$

which is a differential equation for A_2 on the surface. This equation, giving the excess flux per unit length of circumference, is similar to von Kármán's momentum-integral equation. The first term on the right includes the straining effect of the potential flow. If A_2 has a small ripple on it, a compressive strain will cause the ripple to amplify. (This will be seen later to cause a difficulty.) The second term is the potential-flow shear stress which drives the layer.

It remains to calculate the excess pressure at the surface for use in the pressure boundary condition. In (4.16) we estimate the first term on the left and the viscous term to be $O(\delta^2)$ while the rest of the terms are $O(\delta)$, so

$$\left.\begin{aligned} \frac{\partial P}{\partial\zeta} &= \boldsymbol{U}\cdot\frac{\mathrm{D}\hat{\boldsymbol{n}}}{\mathrm{D}t}-\boldsymbol{U}\cdot\boldsymbol{\nabla}\boldsymbol{u}\cdot\hat{\boldsymbol{n}}+O(\delta^2), \\ &= U_t\,\hat{\boldsymbol{t}}\cdot\frac{\mathrm{D}\hat{\boldsymbol{n}}}{\mathrm{D}t}-U_t\,\hat{\boldsymbol{t}}\cdot\boldsymbol{\nabla}\boldsymbol{u}\cdot\hat{\boldsymbol{n}}+O(\delta^2), \\ &= -\frac{\partial A_2}{\partial\zeta}\left(\hat{\boldsymbol{t}}\cdot\frac{\mathrm{D}\hat{\boldsymbol{n}}}{\mathrm{D}t}-\hat{\boldsymbol{t}}\cdot\boldsymbol{\nabla}\boldsymbol{u}\cdot\hat{\boldsymbol{n}}\right)+O(\delta^2), \\ &= \frac{\partial\left[-A_2\left(\hat{\boldsymbol{t}}\cdot\dfrac{\mathrm{D}\hat{\boldsymbol{n}}}{\mathrm{D}t}-\hat{\boldsymbol{t}}\cdot\boldsymbol{\nabla}\boldsymbol{u}\cdot\hat{\boldsymbol{n}}\right)\right]}{\partial\zeta}+O(\delta^2). \end{aligned}\right\} \tag{4.25}$$

Therefore, integrating this into the interior where P and A_2 are zero, we find

$$P = -A_2\left(\hat{\boldsymbol{t}}\cdot\frac{\mathrm{D}\hat{\boldsymbol{n}}}{\mathrm{D}t}-\hat{\boldsymbol{t}}\cdot\boldsymbol{\nabla}\boldsymbol{u}\cdot\hat{\boldsymbol{n}}\right)+O(\delta^3). \tag{4.26}$$

In particular, this gives the excess pressure on the surface itself.

The pressure boundary condition (4.4) at the free surface, with pressure given by (4.8), is

$$\frac{\partial \phi}{\partial t}+\frac{\boldsymbol{u}\cdot\boldsymbol{u}}{2}-P+2R_e^{-1}\hat{\boldsymbol{n}}\cdot\nabla\boldsymbol{u}\cdot\hat{\boldsymbol{n}} = -T'\operatorname{div}\hat{\boldsymbol{n}}, \tag{4.27}$$

where P is given by (4.26) with A_2 to be determined by integrating (4.24).

The motion of points on the surface should be determined from

$$\frac{\mathrm{d}\boldsymbol{r}}{\mathrm{d}t} = \boldsymbol{u}+\boldsymbol{U}, \tag{4.28}$$

with $\boldsymbol{U} = \nabla\times\boldsymbol{A}$. However, while $\boldsymbol{U}$ is not completely known, its normal component can be determined from values of A_2 on the surface by using

$$U_n = \hat{\boldsymbol{n}}\cdot\nabla\times\boldsymbol{A} = \frac{1}{r}\frac{\partial rA_2}{\partial s}. \tag{4.29}$$

But this is enough, since the evolution of a surface is completely determined by the normal component of the velocity. Therefore we shall use

$$\frac{\mathrm{d}\boldsymbol{r}}{\mathrm{d}t} = \boldsymbol{u}+U_n\hat{\boldsymbol{n}} \tag{4.30}$$

instead of (4.28) to evolve the surface shape.

It is desirable, however, that the time derivative in (4.24) follow the same path as the boundary points. Since U_n and A_2 are $O(\delta^2)$ the left-hand side of (4.24) can be replaced by

$$\frac{\partial A_2}{\partial t}+(\boldsymbol{u}+U_n\hat{\boldsymbol{n}})\cdot\nabla A_2 \equiv \frac{\mathrm{d}A_2}{\mathrm{d}t}. \tag{4.31}$$

Then (4.24) may be rewritten as

$$\frac{\mathrm{d}A_2}{\mathrm{d}t} = -(2\hat{\boldsymbol{t}}\cdot\nabla\boldsymbol{u}\cdot\hat{\boldsymbol{t}}+\boldsymbol{u}\cdot\hat{\boldsymbol{r}}/r)A_2+2R_e^{-1}\hat{\boldsymbol{t}}\cdot\nabla\boldsymbol{u}\cdot\hat{\boldsymbol{n}}+O(\delta^3). \tag{4.32}$$

Similarly, using this definition of $\mathrm{d}/\mathrm{d}t$ and (4.21), (4.27) becomes

$$\frac{\mathrm{d}\phi}{\mathrm{d}t} = \frac{\boldsymbol{u}\cdot\boldsymbol{u}}{2}+U_n u_n+P+2R_e^{-1}(\hat{\boldsymbol{t}}\cdot\nabla\boldsymbol{u}\cdot\hat{\boldsymbol{t}}+\boldsymbol{u}\cdot\hat{\boldsymbol{r}}/r)-T'\operatorname{div}\hat{\boldsymbol{n}}. \tag{4.33}$$

Equation (4.26) for P may also be simplified. First note that in the second term $\hat{\boldsymbol{t}}\cdot\nabla\boldsymbol{u} = \partial(\mathrm{d}\boldsymbol{r}/\mathrm{d}t)/\partial s$, neglecting a small term. Changing to Lagrangian variables, $\partial/\partial s = \lambda^{-1}\partial/\partial\xi$, the order of differentiations may be interchanged to get

$$\left.\begin{aligned}\hat{\boldsymbol{t}}\cdot\nabla\boldsymbol{u} &= \lambda^{-1}\frac{\mathrm{d}(\partial\boldsymbol{r}/\partial\xi)}{\mathrm{d}t},\\ &= \lambda^{-1}\frac{\mathrm{d}(\lambda\hat{\boldsymbol{t}})}{\mathrm{d}t},\\ &= \frac{\mathrm{d}\hat{\boldsymbol{t}}}{\mathrm{d}t}+\lambda^{-1}\left(\frac{\mathrm{d}\lambda}{\mathrm{d}t}\right)\hat{\boldsymbol{t}}.\end{aligned}\right\} \tag{4.34}$$

Therefore

$$\left.\begin{aligned}\hat{\boldsymbol{t}}\cdot\nabla\boldsymbol{u}\cdot\hat{\boldsymbol{n}} &= \hat{\boldsymbol{n}}\cdot\frac{\mathrm{d}\hat{\boldsymbol{t}}}{\mathrm{d}t},\\ &= -\hat{\boldsymbol{t}}\cdot\frac{\mathrm{d}\hat{\boldsymbol{n}}}{\mathrm{d}t}.\end{aligned}\right\} \tag{4.35}$$

Then replacing $\mathrm{D}/\mathrm{D}t$ by $\mathrm{d}/\mathrm{d}t$ the excess pressure on the surface becomes

$$P = 2A_2 \hat{\boldsymbol{t}} \cdot \nabla \boldsymbol{u} \cdot \hat{\boldsymbol{n}}. \tag{4.36}$$

The results are summarized below.

Summary of viscous boundary conditions:

$$\frac{\mathrm{d}\boldsymbol{r}}{\mathrm{d}t} = \boldsymbol{u} + U_n \hat{\boldsymbol{n}}, \quad U_n = \frac{1}{r} \frac{\partial r A_2}{\partial s}, \tag{4.37}$$

$$\frac{\mathrm{d}A_2}{\mathrm{d}t} = -(2\hat{\boldsymbol{t}} \cdot \nabla \boldsymbol{u} \cdot \hat{\boldsymbol{t}} + \boldsymbol{u} \cdot \hat{\boldsymbol{r}}/r) A_2 + 2R_e^{-1} \hat{\boldsymbol{t}} \cdot \nabla \boldsymbol{u} \cdot \hat{\boldsymbol{n}}, \tag{4.38}$$

$$\frac{\mathrm{d}\phi}{\mathrm{d}t} = (\boldsymbol{u} + U_n \hat{\boldsymbol{n}}) \cdot (\boldsymbol{u} + U_n \hat{\boldsymbol{n}})/2 + 2A_2 \hat{\boldsymbol{t}} \cdot \nabla \boldsymbol{u} \cdot \hat{\boldsymbol{n}} + 2R_e^{-1}(\hat{\boldsymbol{t}} \cdot \nabla \boldsymbol{u} \cdot \hat{\boldsymbol{t}} + \boldsymbol{u} \cdot \hat{\boldsymbol{r}}/r) - T' \operatorname{div} \hat{\boldsymbol{n}}. \tag{4.39}$$

This set of equations replaces (2.10) and (2.15) as the conditions to determine the shape of the drop and the dipole distribution when weak viscous effects are included. The corrections to the flow are of order R_e^{-1} and we have neglected terms of order $R_e^{-\frac{3}{2}}$. This should be compared with viscous corrections of order $R_e^{-\frac{1}{2}}$ for flows with solid boundaries or two-fluid interfaces.

In physical terms, we have assumed that the thickness of the vortical layer, which is $O(R_e^{-\frac{1}{2}})$, is much smaller than the characteristic length of the motion, which has been taken to be unity. If the motion is perceived as the superposition of a large number of oscillating modes the characteristic length could actually be as small as the shortest resolved wavelength. When $N = 101$ the 50th mode, with 4 nodes per wavelength, is about the limit we can hope to resolve. This has wavelength of about 0.12 units. When $R_e = 2000$, which has been used for a number of computations, the thickness of the vortical layer is about 0.02. So for this worst possible case the condition is more than just marginally satisfied.

The viscous terms have been used for integrations of a 25th-mode test case. The results for small amplitude (10^{-3}) are shown in figure 5(*a*) where decaying oscillations for $R_e = 1000$ are compared to a linearized result from Lamb (1932, §355), in which the amplitude of the nth mode has a decay factor $\exp(-t/\tau)$ with $\tau = R_e/[(n-1)(2n+1)]$ in our units. The comparison is excellent, as it is for Reynolds numbers even as low as 100 where the amplitude decays to zero in about 4 cycles, which is too small for either Lamb's theory or the present equivalent results to be applicable.

A difficulty occurs at higher amplitude. The zigzag instability recurs when the amplitude is 0.02, even when smoothing is used. That is, the viscous term causes the instability to occur in a case that was stable before. This has been traced to the (nonlinear) straining term in (4.38). When this term is removed no instability is seen. It appears that straining by the potential flow can amplify a small zigzag disturbance enough during the compressive part of a cycle that the instability can run to excessively high amplitudes before the stabilizing stretching part of the cycle can counter the growth. This problem was solved by smoothing A_2 in the same manner as for the surface potential. Again this has the same effect as having a fourth-derivative damping term on the right-hand side of (4.38). This compensates (or overcompensates) for the neglected second-derivative viscous term. (That second derivative is negligible when wavelengths are long compared with the thickness of the vortical layer, but we did not count on non-physical 2Δ waves.)

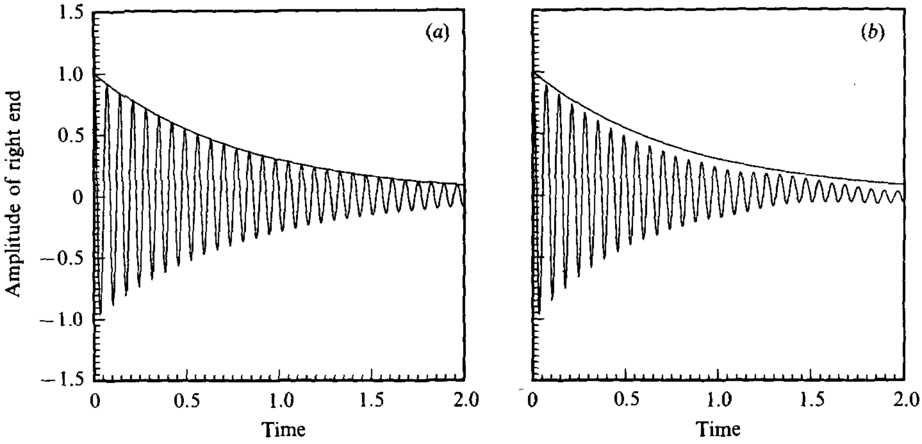

FIGURE 5. Test cases with the 25th mode showing the effect of viscosity. The initial conditions are of the form $\phi = 0, r = 1+\epsilon P_{25}$. The quantity plotted is normalized amplitude, $(z(1)-z_0(1))/\epsilon$; $N = 101$, $\Delta t = 0.005$, $R_e = 1000$. (*a*) $\epsilon = 0.001$, (*b*) $\epsilon = 0.02, D_1 = D_2 = 0.01$.

A test with the 25th mode, with $R_e = 1000$, amplitude $= 0.02$ and with both smoothing factors (the smoothing parameter for A_2 is called D_2) equal to 0.01 is shown in figure 5(*b*). Notice that the oscillations decay somewhat faster than the linear theory would predict. This is almost entirely due to D_1 as has been verified by comparing with computations with $D_1 = 0$ and $D_2 = 0.01$.

An alternative approach is to neglect the destabilizing straining term in (4.38) using

$$\frac{\mathrm{d}A_2}{\mathrm{d}t} = \boldsymbol{u}\cdot\hat{\boldsymbol{r}}A_2/r + 2R_e^{-1}\hat{\boldsymbol{t}}\cdot\nabla\boldsymbol{u}\cdot\hat{\boldsymbol{n}} \tag{4.40}$$

instead. This can be justified for problems with moderate nonlinear effects. The modified equation can be used with D_1 equal to zero, i.e. the viscous terms now stabilize the zigzag instability. We rarely use the equations this way.

5. Nonlinear drop oscillations

In this section we present the results of some long computations with fourth- and fifth-mode initial conditions of type (3.1) with weak viscous effects. We have selected these modes for two reasons. First there are interesting resonant couplings between these modes and others. Secondly, in order to show the effect of small viscosity it is necessary to compute a large number of periods. With fourth-order Runge–Kutta and $N = 101$ we are limited to Δt smaller than 0.0085 for stability reasons (we usually use $\Delta t = 0.005$).

5.1. *Fourth-mode results*

Figure 6 shows typical fourth-mode shapes for about one period computed from initial conditions $r = 1+0.3P_4, \phi = 0$. Figure 7 shows the amplitude and energy results when $R_e = 2000$ and $D_1 = D_2 = 0.01$. In figure 7(*a*) it can be seen that every third amplitude peak is lower than the other two. At first we thought this was a subharmonic resonance caused by the fact that the second mode has a natural frequency one-third that of the fourth mode ($\omega_2^0 = 2, \omega_4^0 = 6$), however the mechanism

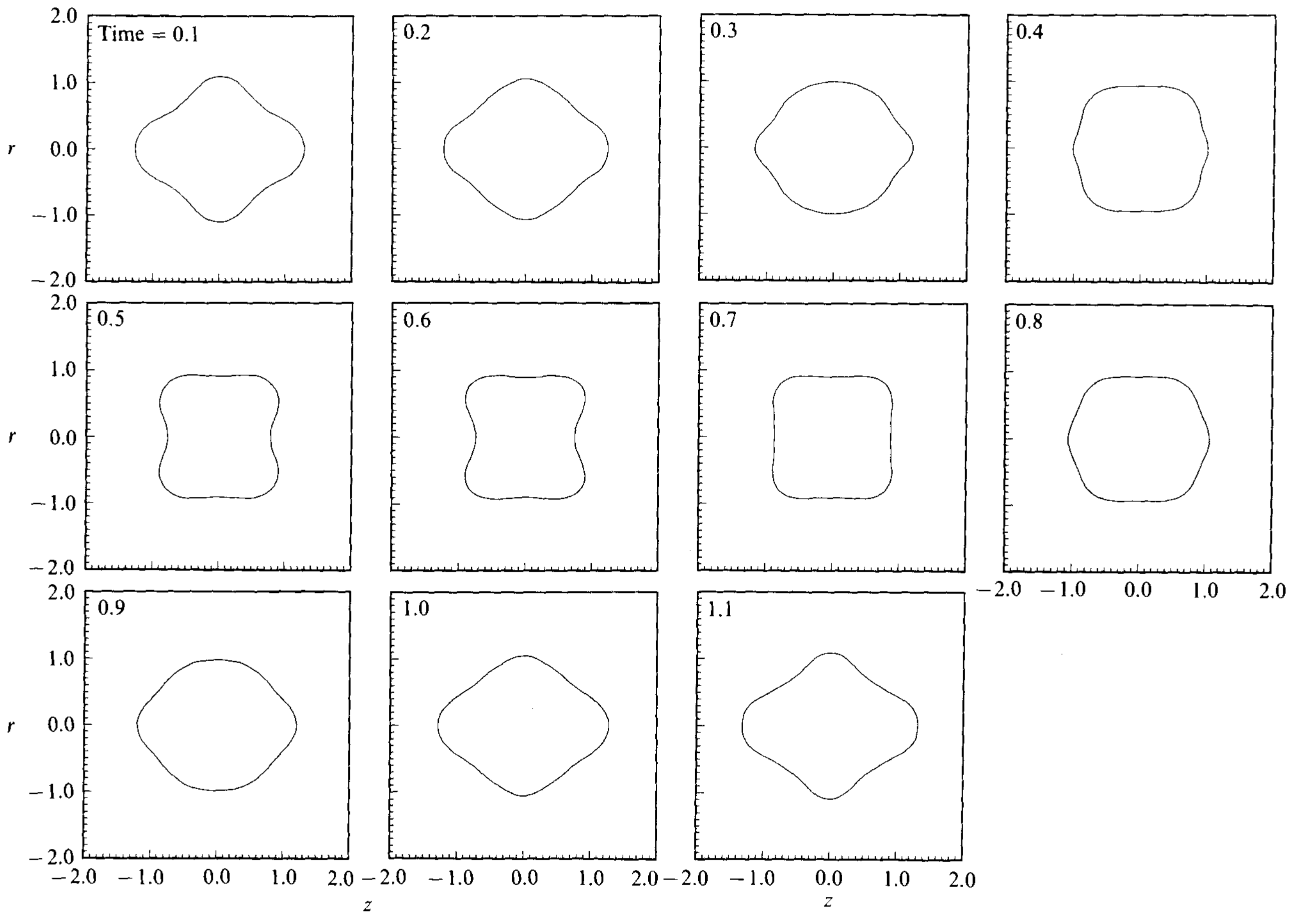

FIGURE 6. Fourth-mode drop shapes over about one period of oscillation. Initial conditions were $\phi = 0, r = 1+0.3P_4$, initial shape not shown; $N = 101, \Delta t = 0.005, D_1 = 0.01$.

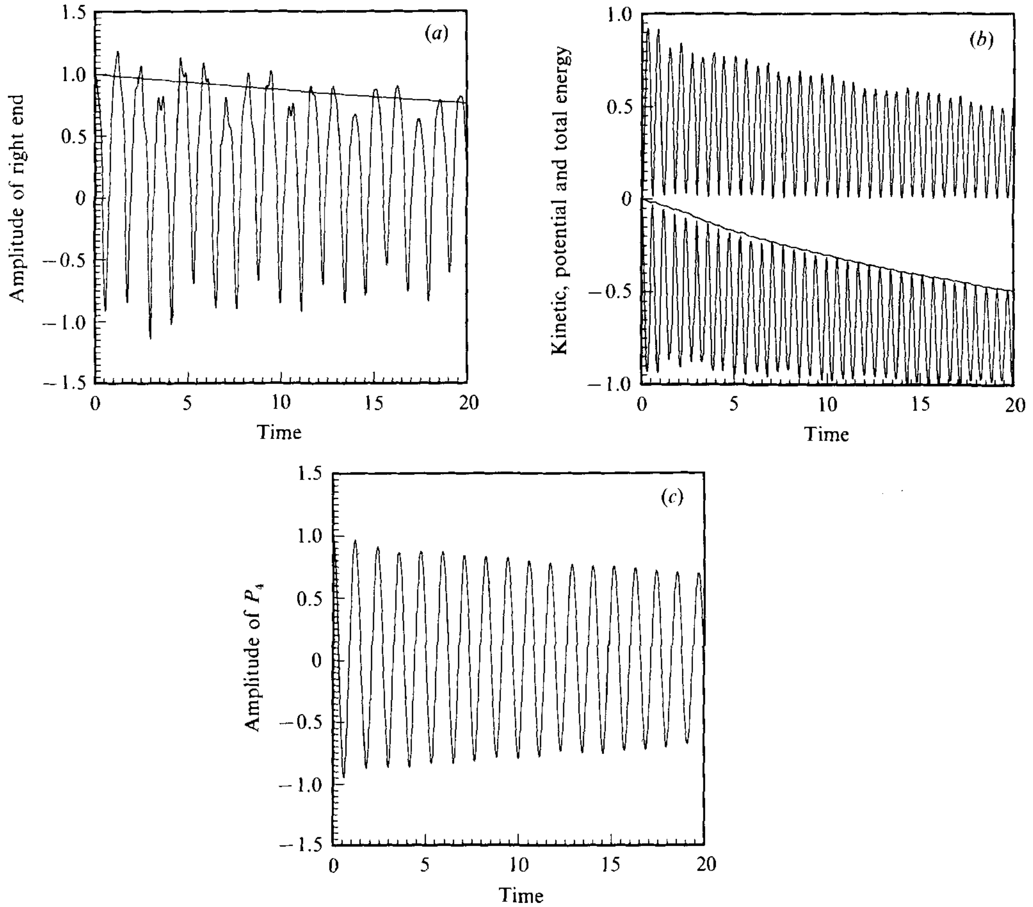

FIGURE 7. Fourth-mode oscillations with same initial conditions as in figure 6, and with $R_e = 2000$ and $D_2 = 0.01$. (*a*) Normalized amplitude of the right end. The amplification factor from the linear theory is also shown. (*b*) The upper oscillation is kinetic energy, the lower one is potential energy with ordinate shifted to start from zero. The non-oscillating curve is the total energy, not a theoretical result. It would be a horizontal curve through zero if there were no viscosity and no errors due to smoothing. (*c*) The amplitude of the fourth mode computed from the drop shape by modal decomposition.

for this is not clear. In order to explore this and other features in more detail we have decomposed the drop shape into its linear modes according to

$$r = 1 + \sum_{j=1}^{\infty} C_n(t) P_n(\cos\Theta), \tag{5.1}$$

using orthogonality of the Legendre polynomials to directly compute

$$C_n = (n+\tfrac{1}{2}) \int_{-1}^{1} (r-1) P_n(\cos\Theta) \,\mathrm{d}\cos\Theta \tag{5.2}$$

by integrating the computed function $r(\Theta, t)$. Since $P_n(\Theta = 0) = 1$ this decomposition has the property

$$\text{Amplitude of the right end} = \sum_{j=1}^{\infty} C_n(t), \tag{5.3}$$

that is, the quantity plotted in figure 7(*a*) is the superposition of all the modal

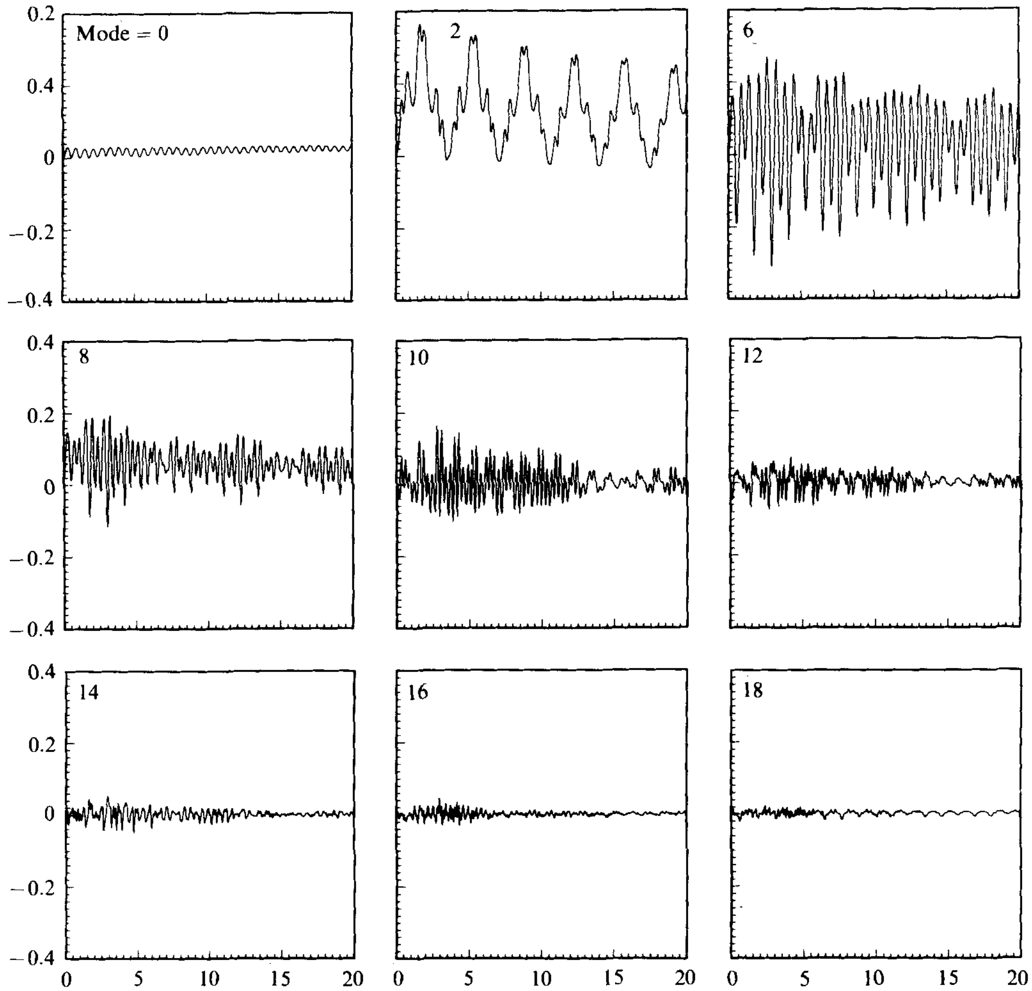

FIGURE 8. Same conditions as for figure 7, showing the remaining non-zero modal amplitudes up to the eighteenth. The sum of all the modal amplitudes adds up to the 'amplitude of the right end' shown in figure 7(*a*).

amplitudes. In figure 7(*c*) the fourth-mode amplitude C_4 is shown at the same scale as in figure 7(*a*), and in figure 8 all the even modes up to the eighteenth are shown at an enlarged scale. All the modal amplitudes have been divided by the initial amplitude of the fourth mode.

Tsamopoulos & Brown (1983) have studied non-viscous drop oscillations analytically by expanding to second order in amplitude. The problem they solve is a little different from our initial-value problem. They look for strictly periodic oscillations in which the amplitude is defined as the coefficient of $P_n(\cos\Theta)\cos\omega_n t$ (other terms proportional to P_n are time orthogonal to $\cos\omega_n t$). They do this for $n = 2, 3, 4$. For the fourth mode they find the result

$$\left.\begin{aligned} r = {} & 1+\epsilon P_4\cos T+\tfrac{1}{2}\epsilon^2(-0.222\cos^2 T \\ & +1.290(1-0.219\cos 2T)P_2+0.463(1-0.974\cos 2T)P_4 \\ & +0.385(1-4.311\cos 2T)P_6+0.598(1-0.299\cos 2T)P_8), \\ T = {} & \omega_4 t, \quad \omega_4=\omega_4^0(1-1.457\epsilon^2+O(\epsilon^4)), \end{aligned}\right\} \qquad (5.4)$$

in which only the zeroth, second, fourth, sixth, and eighth modes are excited at second order and have modal amplitudes that oscillate with twice the primary frequency. This is quite different from what we observe. For instance the second mode in figure 8 has a strong component that oscillates with the natural frequency of the second mode. The smaller ripple superimposed on this is at double the fourth-mode frequency. The difference is caused by the difference in the problems. We will return to their problem later in a separate subsection.

In our case the second-mode excitation appears to be caused by second-order quadratic coupling with the fundamental fourth mode. The equation for the second mode, in an intuitive physical picture, would be like a linear oscillator with natural frequency ω_2, with a driving term that is the square of the fourth mode. The Fourier decomposition of the driving term has a contribution that is sinusoidal at twice the fourth-mode frequency and it also has a constant contribution. The constant driving-force part has a solution proportional to $\epsilon^2(1-\cos\omega_2 t)$ (it has to be initially zero with zero derivative). This is a second-mode oscillation which is offset from zero amplitude as observed in the figure. It is this second mode that causes every third peak to be lower in figure 7(*a*) and it is not caused by subharmonic resonance. The fact that the frequencies are related by a factor of three is incidental except as it effects the appearance of the figure.

The zeroth mode is excited at twice the frequency of the fourth mode, as is the sixth mode. However there also appears to be a near-harmonic resonance in the sixth mode with its characteristic beats. The linearized natural frequency of the sixth mode is $\omega_6^0 = 10.95$, which is noticeably less than double the linearized frequency of the fourth mode. However, because the mode frequency softens with amplitude, $\omega_4 \approx 5.46$ (obtained by counting the peaks in figure 7*c*) is very nearly half of ω_6^0. Therefore there appears to be an opportunity for second-order resonant coupling between the fourth and sixth modes through the quadratic nonlinearities. (However the presence of the beats means that the frequencies are not quite close enough for resonance.) Also we note that the deep troughs in this figure are at the fourth-mode frequency, indicating that there is superposition of a term resulting from third-order coupling through these nonlinearities.

The basic frequency seen in the eighth mode is nearly its linearized frequency ($\omega_8 = 16.0, \omega_8^0 = 16.73$). It appears to be excited by the same mechanism acting on the second mode as is suggested by the characteristic offset from zero in the figure; however the presence of beats indicates near-resonant coupling in addition. The deeper troughs in the eighth-mode figure coincide with the troughs of the fourth mode. A check shows that the eighth mode has about three times the frequency of the fourth. Therefore we think this is another situation where third-order quadratic coupling is important, probably involving the sixth mode also.

The tenth-mode frequency is near its linear frequency and is close to $4\omega_4$. Therefore with the apparent beat this looks like third-order or fourth-order near-quadratic resonance. The remaining modes are all smaller than those discussed above. Each appears to have a component near its linearized frequency which damps out due to viscous effects (more rapidly for the higher modes).

A computation with zero viscosity and $D_1 = 0.01$ was made for comparison and to isolate the effect of the D_1 smoothing coefficient. The results are not shown. It was found that $D_1 = 0.01$ caused an energy loss of about 5% of the maximum kinetic energy in this fairly long run. If this loss is representative of the loss in the viscous run as well, then the smoothing loss is only about 10% of the real viscous loss. The smoothing loss in amplitude is not noticeable at all. By counting the peaks in the non-viscous-amplitude figure we find the angular frequency is $\omega_4 = 5.26$, a little

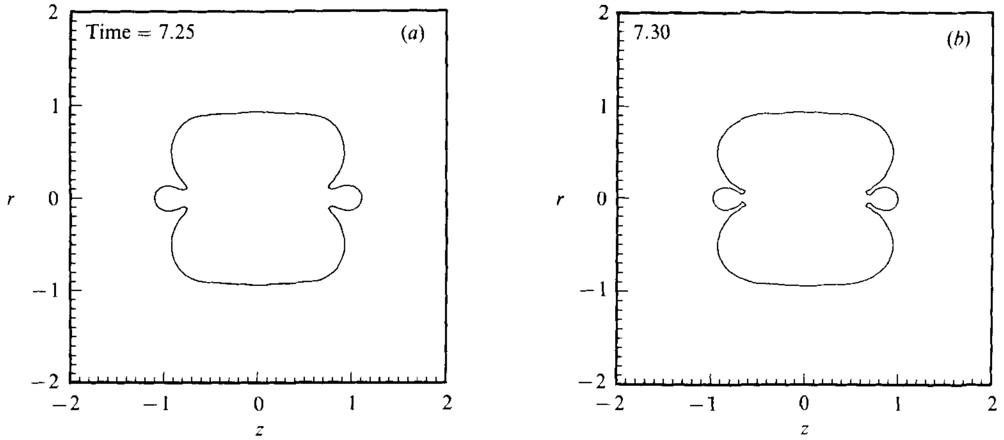

FIGURE 9. Large-amplitude fourth-mode shape just before computation failure. Initial conditions $\phi = 0, r = 1+0.4P_4$; non-viscous. This occurs after about five oscillations.

lower than for the viscous case and lower than the linear value, $\omega_4^0 = 6$, as expected. The frequency formula given by Tsamopoulos & Brown (1983) yields a comparable value, $\omega_4 = 5.21$. More direct comparison with their work is pursued below.

Computations with larger amplitudes have also been attempted. When the initial conditions are $r = 1+0.35P_4, \phi = 0$ we find results similar to those already shown, with the second mode a little more pronounced. When the amplitude is as large as 0.4 the computations fail. Figure 9 shows the drop shape after about five oscillations, just before failure. This occurs when the sixth-mode amplitude is near a maximum while the fourth mode is approaching a minimum. The computation fails when the sides of the small droplets touch the main body.

5.2. *Direct comparison with Tsamopoulos & Brown*

In order to compare more directly to Tsamopoulos & Brown's fourth-mode results we have computed several non-viscous cases using their result (5.4) to provide the proper initial conditions for a strictly periodic solution. The appropriate initial conditions are

$$\left.\begin{aligned} r &= 1+(\epsilon+0.006\epsilon^2)P_4+\epsilon^2(-0.111+0.504P_2-0.638P_6+0.210P_8),\\ \phi &= 0. \end{aligned}\right\} \qquad (5.5)$$

We have done computations with $\epsilon = 0.05$, $\epsilon = 0.1$ and $\epsilon = 0.2$ with results for modal amplitudes that are essentially within the second-order accuracy of their theory, though the third-order errors are certainly very noticeable at $\epsilon = 0.2$ and the second-order terms in the eighth mode, which are relatively small, are dominated by the third-order terms even for $\epsilon = 0.05$. For $\epsilon = 0.2$ the sixth and eighth modes look much like those in figure 8 reduced by about 30%. The tenth mode, which should be third order, is about half as large as the eighth. The second mode has a much reduced contribution (compared with figure 8) from the natural second-mode frequency. We find that the fourth-mode frequency, for $\epsilon = 0.1$ and $\epsilon = 0.2$, is in agreement with the theory within ±0.01, which is our reading accuracy.

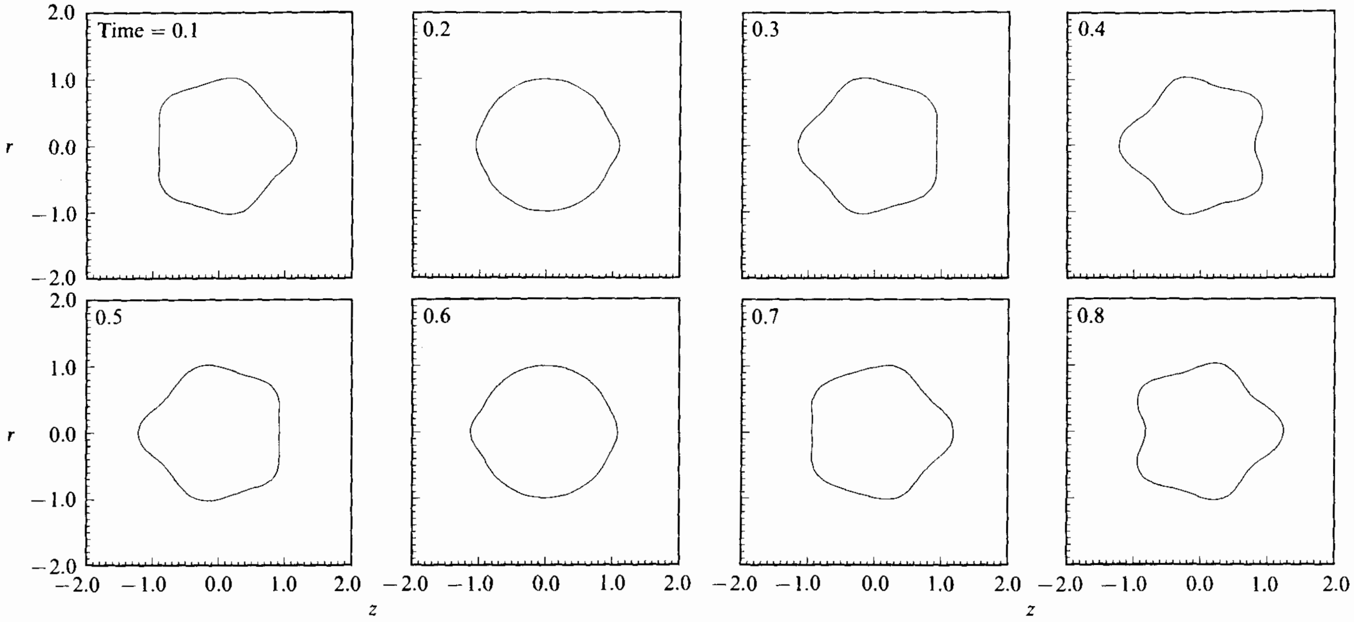

FIGURE 10. Fifth-mode drop shapes over about one period of oscillation. Initial conditions were $\phi = 0, r = 1+0.2P_5$, initial shape not shown; $N = 101, \Delta t = 0.005, D_1 = 0.01$.

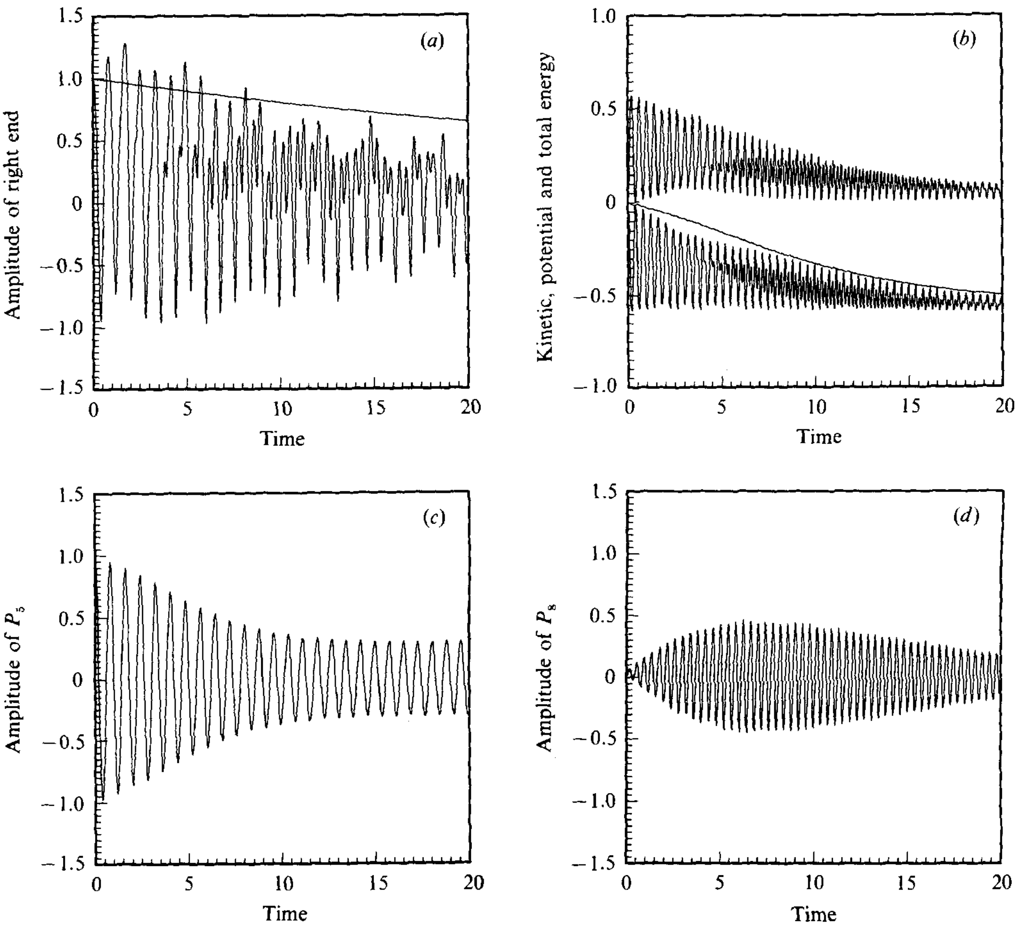

FIGURE 11. Fifth-mode oscillations with the same initial conditions as in figure 10 but with $R_e =$ 2000 and $D_2 = 0.01$. (*a*) Normalized amplitude of the right end showing resonance with the eighth mode which has double the (linearized) natural frequency. (*b*) The generation and decay of the eighth mode is seen more clearly in these energy traces. (*c*) Modal amplitude of the fifth mode. (*d*) Modal amplitude of the eighth mode.

5.3. *Fifth-mode results*

Figure 10 shows typical fifth-mode shapes for about one period computed with initial conditions $r = 1+0.2P_5, \phi = 0$. Figure 11 shows the results when $R_e = 2000$ and $D_1 = D_2 = 0.01$. In figure 11 (*a*) an oscillation with frequency double the fundamental frequency becomes apparent after a short time. This is clearly seen in the energy figure, and is even more clearly seen in figure 11 (*c* and *d*), which show the modal amplitudes of the fifth and eighth modes. This is caused by second-order quadratic coupling with the eighth mode which has linear frequency double that of the fifth mode ($\omega_5^0 = (70)^{\frac{1}{2}}, \omega_8^0 = 2(70)^{\frac{1}{2}}$). This mode coupling was pointed out and analysed by Natarajan & Brown (1986). They showed, for non-viscous axially symmetric drop oscillations, that when there is initially some energy in each of these two modes there will be a slow periodic transfer of energy back and forth between the modes. In the limit when all of the energy is initially in the fifth mode, as in our computation, they show that the period goes to infinity and there will be an irreversible slow transfer of energy to the eighth mode. (They also show that this axially symmetric problem

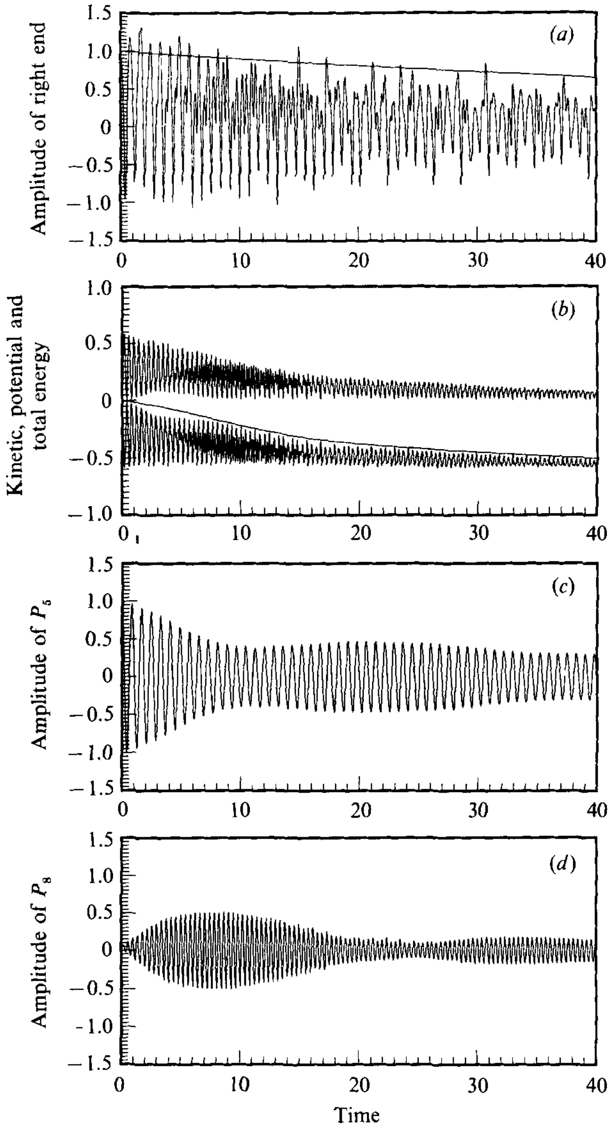

FIGURE 12. Same as figure 11 with $R_e = 4000$ and with twice the integration time. This shows a decaying slow oscillation between the fifth and eighth modes.

is unstable to non-axially symmetric disturbances. The instability generates finite-amplitude circumferential waves. Three-dimensional computations are planned for future work.) From the figures we see what appears to be the beginning of a slow transfer to the eighth mode which is impeded by the larger viscous damping at this higher frequency. In fact the damping is so great that the eighth mode begins to die out before the transfer is complete and we end up with most of the remaining energy in the fifth mode. This case was rerun with $N = 61$ and $\Delta t = 0.01$ for double the time interval to verify that the eighth mode does continue to decay.

A long, high quality computation ($N = 101, \Delta t = 0.005$) was made with a smaller viscosity, $R_e = 4000$. The results in figure 12 show that with the smaller viscous damping the initial transfer to the eighth mode is about the same before it begins to

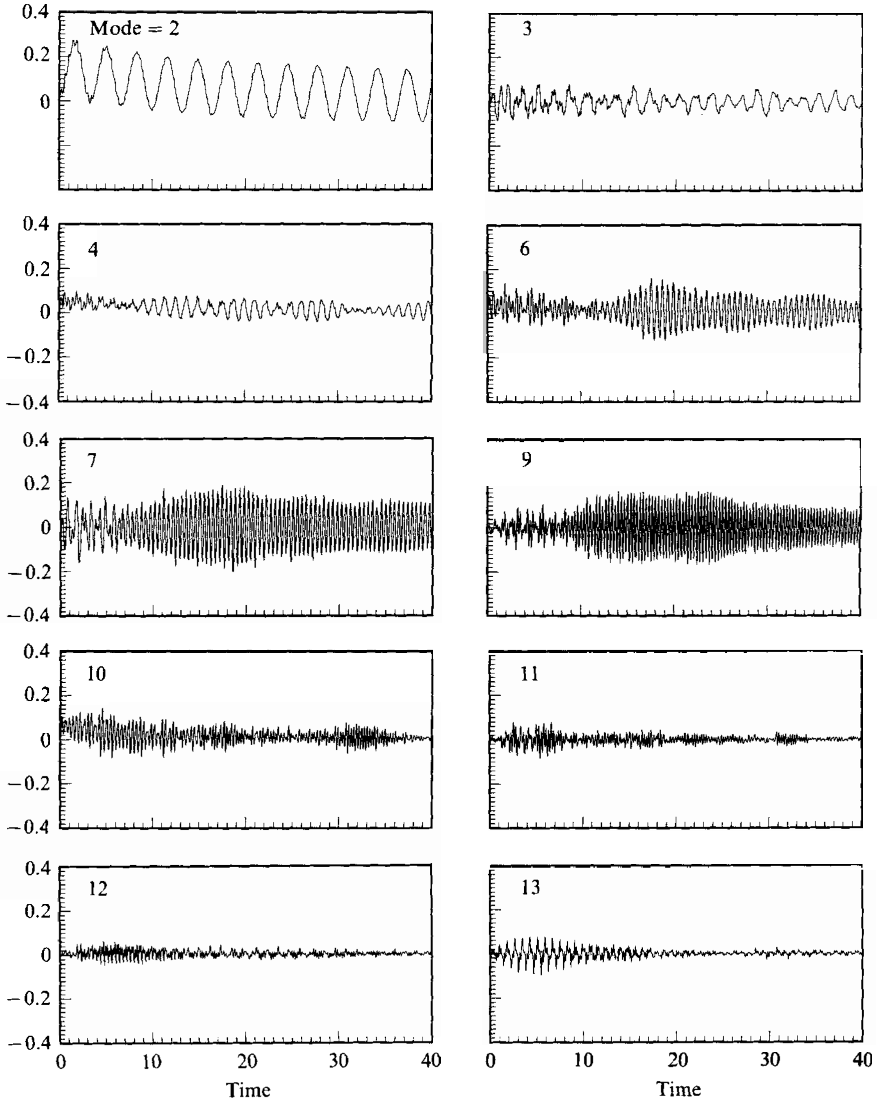

FIGURE 13. Same conditions as figure 12 showing a number of other modal amplitudes.

decay. Therefore the viewpoint that the considerable undershoot of full transfer to the eighth mode is purely a viscous effect must be wrong. The energy result in figure 12(*b*) would seem to indicate that the eighth mode again decays away completely; however the mode decomposition in figure 12(*d*) shows in fact that it slowly increases again before decaying out. This looks more like viscous damping of the slow periodic case that results when energy is initially in both modes, despite the fact that all the energy was initially in the fifth mode. We believe that this feature is not caused by viscosity but is a finite-amplitude effect. Several runs with smaller ϵ, and zero viscosity, show that a greater fraction of the energy is transferred to the eighth mode before it decreases. When $\epsilon = 0.1$ the amplitude of P_8 increased to what looked like a maximum at 70% of the initial P_5 by the end of the run, at $t = 20$. The problem is that as ϵ is made smaller the timescale for the slow variation becomes longer (like ϵ^{-1}) and therefore it is difficult to know whether the amplitude would continue to increase without making longer and longer runs with smaller and smaller ϵ. With any small viscosity, however, the limit as ϵ tends to zero would ultimately be dominated by viscosity as the viscous decay time becomes shorter than the timescale for the slow amplitude modulation.

In figure 13 the remaining modes are shown. The second mode is excited at its natural frequency by the same mechanism discussed for fourth-mode oscillations. The seventh and ninth modes are also excited at their natural frequencies, but apparently by a different mechanism since the oscillations are symmetric about the origin.

We have done additional computations with larger amplitudes. The case $r = 1+0.25P_5, \phi = 0$ gives results much like those already seen. When the amplitude is 0.3 the computation fails in a manner similar to the failure of the large-amplitude fourth-mode computations.

6. Conclusions

A numerical boundary-integral method has been developed which is applicable to the axially symmetric motion of large liquid drops. The method shows considerable flexibility. Figure 4 shows that it may be used for extremely large motions and suggests its usefulness in further studies of drop or jet breakup.

A novel method of including the effects of small viscosity has been derived in which these effects are adapted to the boundary-integral method in the form of modified surface boundary conditions which produce higher-order corrections to the potential flow. In earthbound flows of contained liquids with free surfaces the main source of viscous effects is from boundary layers at the solid surfaces, with much smaller contributions from the free surface. In zero-gravity containerless flows the only source of damping is the latter weak free-surface contribution, which therefore takes on a greater significance. A rather large effect of small viscosity is seen in figures 11, 12 and 13 where resonant energy transfer from the fifth mode to the higher (double) frequency eighth mode is modified because of the larger effect of viscosity on the higher mode. We see this as similar to turbulent flow where energy is transferred to smaller scales where it is dissipated.

The effect of viscosity was much smaller in the fourth-mode computations. It is seen mainly as a more rapid decay of the higher-mode content of the oscillations. At zero viscosity we found that the finite-amplitude frequency shift of the fourth mode was in agreement with the prediction of Tsamopoulos & Brown (1983).

One of the authors (T.S.L.) wishes to acknowledge support from NASA/Ames Research Center Director's Discretionary Fund. Contract NCA2-114, during the summers of 1986 and 1987.

REFERENCES

ABRAMOWITZ, M. & STEGUN, I. A. 1972 *Handbook of Mathematical Functions*. Washington, DC: Government Printing Office.

ALONZO, C. T. 1974 The dynamics of colliding and oscillating drops. In *Proc. Intl Colloq. on Drops and Bubbles* (ed. D. J. Collins, M. S. Plesset & M. M. Saffren), pp. 139–157. Jet Propulsion Laboratory.

BAKER, G. R., MEIRON, D. I. & ORSZAG, S. A. 1980 Vortex simulations of the Rayleigh–Taylor instability. *Phys. Fluids* **23**, 1485–1490.

BAKER, G. R., MEIRON, D. I. & ORSZAG, S. A. 1982 Generalized vortex methods for free-surface flow problems. *J. Fluid Mech.* **123**, 477–501.

BAKER, G. R., MEIRON, D. I. & ORSZAG, S. A. 1984 Boundary integral methods for axisymmetric and three-dimensional Rayleigh–Taylor instability problems. *Physica* **12 D**, 19–31.

BATCHELOR, G. K. 1967 *An Introduction to Fluid Dynamics*. Cambridge University Press.

BENNER, R. E. 1983 Equilibria, stability and bifurcations in the physics of fluid interfaces. Ph.D. thesis, University of Minnesota, Minneapolis.

CARRUTHERS, J. R. & TESTARDI, L. R. 1983 Materials processing in the reduced-gravity of space. *Ann. Rev. Mater. Sci.* **13**, 247–278.

DE BERNADINIS, B. & MOORE, D. W. 1985 A ring-vortex representation of an axi-symmetric vortex sheet. In *1985 ICASE Workshop on Vortex Dominated Flows*, 33–43.

DOMMERMUTH, D. G. & YUE, D. K. P. 1987 Numerical simulations of nonlinear axisymmetric flows with a free surface. *J. Fluid Mech.* **178**, 195–219.

FOOTE, G. B. 1973 A numerical method for studying simple drop behavior: simple oscillation. *J. Comp. Phys.* **11**, 507–530.

FROMM, J. E. 1984 Numerical calculation of the fluid dynamics of drop-on-demand jets. *IBM J. Res. Dev.* **28**, 322–333.

HASEGAWA, H. & YAMASHITA, S. 1986 Finite amplitude waves on an elastic plate horizontally separating two different fluid streams. *Bull. JSME* **29**, 787–784.

JASWON, M. A. & SYMM, G. T. 1977 *Integral Equation Methods in Potential Theory and Elastostatics*. Academic.

KELLOGG, O. D. 1953 *Foundations of Potential Theory*. Dover.

KRASZNY, R. 1986 A study of singularity formation in a vortex sheet by the point-vortex approximation. *J. Fluid Mech.* **167**, 65–93.

LAMB, H. 1932 *Hydrodynamics*, 6th edn. Cambridge University Press.

LONGUET-HIGGINS, M. S. & COKELET, E. D. 1976 The deformation of steep surface waves on water I. A numerical method of computation. *Proc. R. Soc. Lond.* A **350**, 1–26.

MIKSIS, M. J., VANDEN-BROECK, J.-M. & KELLER, J. B. 1982 Rising bubbles. *J. Fluid Mech.* **123**, 31–41.

MILLER, C. A. & SCRIVEN, L. E. 1968 The oscillations of a droplet immersed in another fluid. *J. Fluid Mech.* **32**, 417–435.

MOORE, D. W. 1962 The boundary layer on a spherical gas bubble. *J. Fluid Mech.* **16**, 161–176.

MOORE, D. W. 1982 A point vortex method applied to interfacial waves. In *Vortex Motion* (ed. H. G. Hornung & E.-A. Muller), pp. 97–105.

NATARAJAN, R. & BROWN, R. A. 1986 Quadratic resonance in the three-dimensional oscillations of inviscid drops with surface tension. *Phys. Fluids* **29**, 2788–2797.

PULLIN, D. I. 1982 Numerical studies of surface-tension effects in nonlinear Kelvin–Helmholtz and Rayleigh–Taylor instability. *J. Fluid Mech.* **119**, 507–532.

RAYLEIGH, J. W. S. 1879 On the capillary phenomena of jets. *Proc. R. Soc. Lond.* **29**, 71–97.

SAFFREN, M., ELLEMAN, D. D. & RHIM, W. K. 1981 Normal modes of a compound drop. In *Proc. Second Intl Coll. Drops and Bubbles* (ed. D. H. Lecroissette), pp. 7–14.

TRINH, E. & WANG, T. G. 1982 Large-amplitude free and driven drop-shape oscillations: experimental observations. *J. Fluid Mech.* **122**, 315–338.

TRINH, E., ZWERN, A. & WANG, T. G. 1982 An experimental study of small-amplitude drop oscillations in immiscible systems. *J. Fluid Mech.* **115**, 453–474.

TSAMOPOULOS, J. A. & BROWN, R. A. 1983 Nonlinear oscillations of inviscid drops and bubbles. *J. Fluid Mech.* **127**, 519–537.

WEATHERBURN, C. E. 1927 *Differential Geometry of Three Dimensions*. Cambridge University Press.